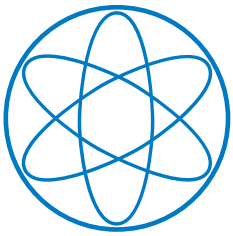

UNIVERSITÉ DE GENÈVE

Technische Universität München

Fakultät für Physik

Faculté des sciences
Ecole de Physique

Master's Thesis

Irène Cucchi

Laser ARPES investigation of the semi-metallic transition metal dichalcogenides WTe_2 and $MoTe_2$

Dr. Rudi Hackl (Walther Meissner Institut)
Prof. Felix Baumberger (University of Geneva)

Garching, 28. Juli 2016

Abstract

The dimensionality of materials strongly influences their fundamental properties. The most striking example is graphene, an atomically thin sheet of graphite showing a wide variety of intriguing phenomena such as the presence of massless Dirac fermions crossing the chemical potential, and, when a gap is induced, a zero field quantum Hall effect. This has motivated the exploration of other layered materials, such as transition metal dichalcogenides (TMDs), strongly anisotropic van der Waals bonded crystals that can be exfoliated to monolayer thickness, and whose exciting properties attracted the interest of chemists, physicists and engineers. Among them, WTe_2 shows the largest magnetoresistance known to date and is theoretically predicted to be a new type of Weyl semimetal, called type II. Type II Weyl fermions are the left or right chiral projections of a massless Dirac fermion that breaks Lorentz invariance. Their presence in condensed matter can be inferred from the observation of characteristic surface states linking the projection of the Weyl nodes. $MoTe_2$, the sister compound of WTe_2, is also predicted to be a type II Weyl semimetal, and also shows a large magnetoresistance. This raised tremendous interest both for fundamental research and for potential applications in hard drives and magnetic sensors using the large magnetoresistance and in quantum computing and low power devices exploiting the anomalous topological properties. Angle Resolved Photoelectron Spectroscopy (ARPES) is a powerful technique to probe the surface band structure of materials which makes it an ideal tool to explore the topological properties of semi-metallic TMDs. In this thesis, I will present an experimental study of WTe_2, $MoTe_2$ and the intermediate solid solution $Mo_xW_{1-x}Te_2$.

Contents

Part I
Introduction

1 Materials

1.1 Materials description

Transition metal dichalcogenides (TMDs) are in the form MX_2, with M a transition metal atom of groups 1 to 4 (in our case, Molybdenum Mo or tungsten W) and X a Chalcogen atom (in our case, Tellurium Te), as highlighted in figure 1. Some elements, like Co or Ir, are only partially highlighted, because only some dichalcogenides form a layered structure [1]. Those dichalcogenides can be insulating like HfS_2, semiconducting like MoS_2, semi-metallic like WTe_2 and $MoTe_2$, and truly metallic like NbS_2.

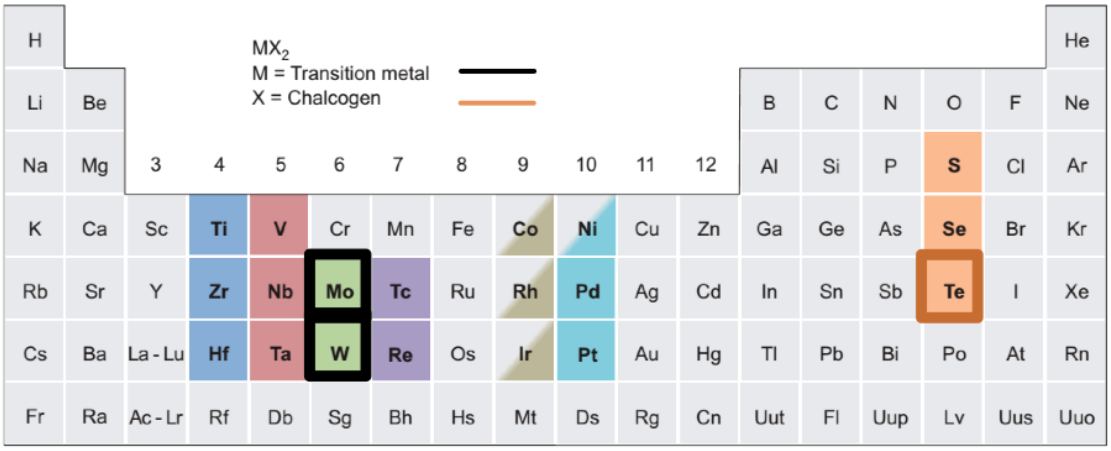

Figure 1: Mo, W and Te, and elements in the periodic table that predominantly crystallize in a layered structure to form TMDs, from [1].

The electronic configuration of the single atoms are written below:
W (Z=74) : [Xe] $4f^{14}$ $5d^4$ $6s^2$
Mo (Z=42): [Kr] $4d^5$ $5s^1$
Te (Z=52): [Kr] $5s^2$ $4d^{10}$ $5p^4$

Te can have an oxidation state of + 4, + 6 or -2 and both Mo and W can have an oxidation state between +2 and + 6 [2]. When crystallized to form a TMD, Te takes an oxidation state of - 2 and Mo and W an oxidation state of +4. Thus the unfilled orbitals should be 4d for Mo and 5d for W.

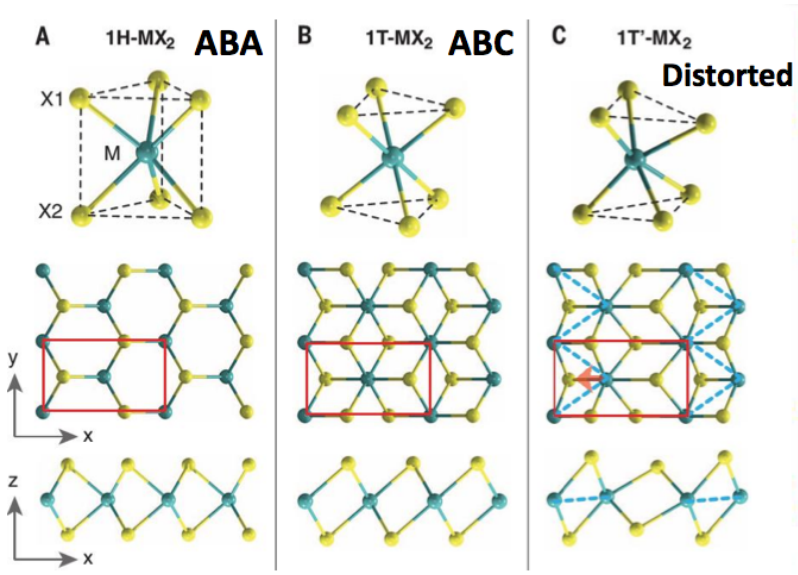

Figure 2: The different structures of WTe_2 , from [3]. The left structure (A) is trigonal prismatic D_{3h}, whereas the middle structure (B) is octahedral O_h or trigonal antiprismatic D_{3d}. The right structure (C) is a distorted version of the 1T structure shown in (B).

In WTe_2 and in $MoTe_2$, two layers of buckled Te atoms are bound together by W or Mo atoms. The interlayer M-Te bond is covalent (M is Mo or W), whereas the resulting three atoms thick layers are then stacked along the c-axis with van der Waals interaction. As a result, the material has a structural anisotropy and preferably cleaves by breaking the van der Waals interaction.

In TMDs, the most common structure is the trigonal prismatic 2H phase, with a hexagonal structure containing two X-M-X units per unit cell, as shown in figure 2(A). The 1T phase can be understood as trigonal antiprismatic structure, with two centrosymmetric tetrahedra sharing the transition metal atom, or as an octahedral phase, with the transition metal atom in octahedral coordination with the chalcogen atoms. In the monoclinic 1T' structure (figure 2(C)), the octahedra surrounding each W or Mo atom is distorted to accommodate the W or Mo atoms. This is due to the formation of M-M bonds: the layers are formed of pseudo-hexagons and the metallic chains have a zigzag form [4]. $MoTe_2$ can be found in the 1T' structure at room temperature, as shown by reference [4] with scanning transmission electron microscopy.

The temperature dependence of the electrical resistivity of the monoclinic $MoTe_2$ shown in figure 3 confirm the semi-metallic behavior of this phase. The hysteresis suggests a structural phase transition at ≈ 240 K, from the 1T' to the Td phase, described schematically in figure 4. Single X-Ray Diffraction measurements performed at 120 K confirm the Td struc-

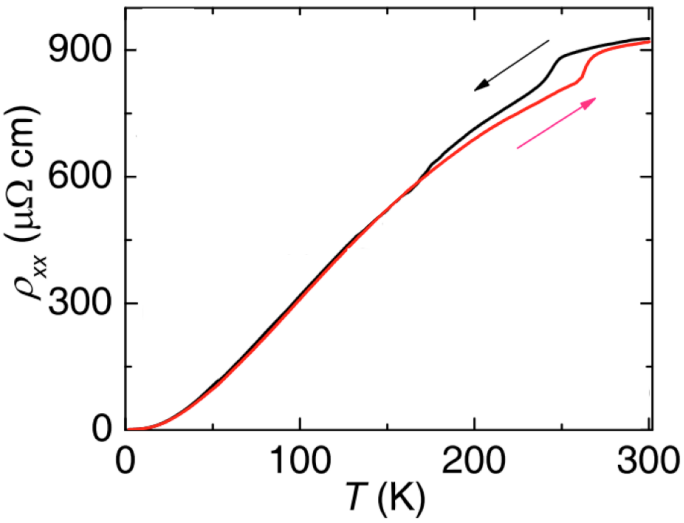

Figure 3: Longitudinal resistivity ρ_{xx} of the semi-metallic $MoTe_2$ as a function of temperature (the red curve and the black curve for a temperature increase and decrease, respectively). The hysteresis anomaly at $\approx$ 240 K is associated with the structural phase transition from the monoclinic 1T' at high temperature to the orthorhombic Td structure at low temperature, from [5].

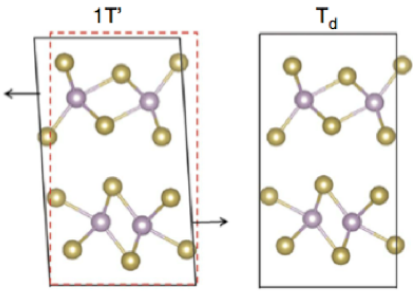

Figure 4: The difference between the 1T' and the Td structure of $MoTe_2$, from [4]. From the 1T' structure, the three atoms thick layers shift relatively to the neighboring ones to form the Td structure.

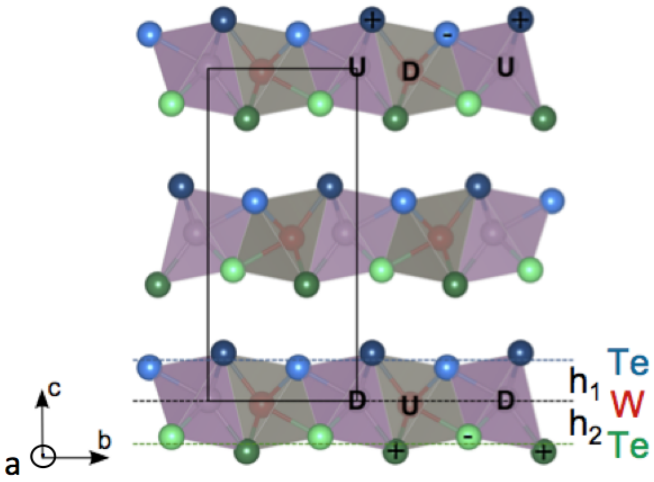

Figure 5: Side view of the orthorhombic crystal structure of WTe_2, with the rectangle indicating the unit cell, from [6]. The distance of the W layer from the upper and lower Te layer is not the same, forming two inequivalent cleaving surfaces.

ture of $MoTe_2$ at low temperature [4]. During this first-order phase transition, the three atoms thick layers shift one with respect to the other to form an orthorhombic structure, close to the 1T' structure, but with a higher symmetry. At low temperature, where the measurements are done, the Td phase is shared by both semi-metallic WTe_2 and $MoTe_2$. As a result, this is mainly the phase I will refer to throughout the thesis, unless it is specified otherwise.

With this structure, WTe_2 and $MoTe_2$ belong to the non-centrosymmetric $Pmn2_1$ space group, where there are two symmetry operations: one mirror symmetry in the (bc) plane and one glide plane formed by the reflection in the (ac) plane and a translation by (0.5, 0, 0.5). There is no mirror symmetry parallel to the (ab) plane. Specifically, the distance h_1 and h_2 between the Mo or W layer with respect to one Te layer or the other is different, as shown in figure 5. This leads to the existence of two inequivalent (001) cleaving surfaces.

1.2 Bulk properties

Thanks to the wide range of physical properties present in 2D materials, such as graphene [7], TMDs, naturally present in layered form, have recently gained interest. At first, the discovery of a sizable band gap in some TMDs such as MoS_2 or WS_2 have made them good candidates for electronic devices such as 2D field effect transistors, photovoltaic panels and light emitting diodes. TMD semiconductors also display properties of interest in fundamental physics, such as charge density waves (CDW), superconductivity and the

valley Hall effect [8].

The semi-metals WTe_2 and $MoTe_2$ illustrate that also metallic TMDs can show interesting behaviors. They exhibit extremely large magnetoresistance and both of them show superconductivity, at ambiant pressure for $MoTe_2$, and at higher pressures for WTe_2.

Superconductivity Qi *et al.*[4] have investigated the transport properties of $MoTe_2$ in the 2H, the 1T' and the Td phase under different pressure. The electrical resistivity measurements at ambient pressure show a superconducting transition at 0.10 K with an onset at 0.25 K for the Td phase, as shown in figure 6(a), whereas no traces of superconductivity are found in the semiconducting 2H phase. Using a miniature diamond high-pressure cell, the electrical resistivity as a function of temperature has been examined for pressures ranging from 0.8 GPa to 11.7 GPa in figure 6(b) and for pressures ranging from 11.7 GPa to 34.9 GPa in figure 6c, indicating a maximum temperature transition to the superconducting phase of 8.2 K for a pressure of 11.7 GPa, more than 30 times the onset temperature found at ambient pressure. These results are confirmed by susceptibility measurements revealing the Meißner-Ochsenfeld effect at temperatures lower than Tc for the different pressures [4].

Kang *et al.* [9] have characterized the electrical resistivity for WTe_2 single crystals in the orthorhombic phase for pressures ranging from 0.3 to 24.0 GPa by applying hydrostatic pressure at zero magnetic field. Figure 7 shows zero electrical resistance below 5 K for these pressures, as emphasized by the inset.

Magnetoresistance The magnetoresistive effect is the change of a material's longitudinal resistance when a magnetic field is applied. WTe_2 is known to exhibit the largest magnetoresistance known to date [3]. A derivation of the magnetoresistance in the Drude model and in the semi-classical model point out the uniqueness of WTe_2.

In his model for electrical conduction, Drude considers metals as a classical gas of negatively charged electrons in an environment of positively charged ions and, as such, applies the kinetic theory of gases to study the electron behavior. The positive charges are heavy and are considered immobile, whereas conduction electrons move freely through the metal. In this model, the electron-electron interaction is neglected (independent electron approximation), and the action of the lattice ions is taken into account by adding a frictional damping term in the equation of motion for the electron momentum. In the presence of externally applied fields, each electron is taken to move as determined by Newton's law of motion in the presence of those fields. For this discussion of the Drude model and of the semi-classical model of electron dynamics, I will follow Chapter 1 and Chapter 12 of reference [10].

We consider an electron moving in a electric field $\mathbf{E} = \mathrm{E}_x\mathbf{u}_x$ and magnetic field $\mathbf{B} = \mathrm{B}_z\mathbf{u}_z$. As such, it will be subjected to the Lorentz force, $\mathbf{F}_L = \mathrm{q}(\mathbf{E} + \mathbf{v} \times \mathbf{B})$. Assuming

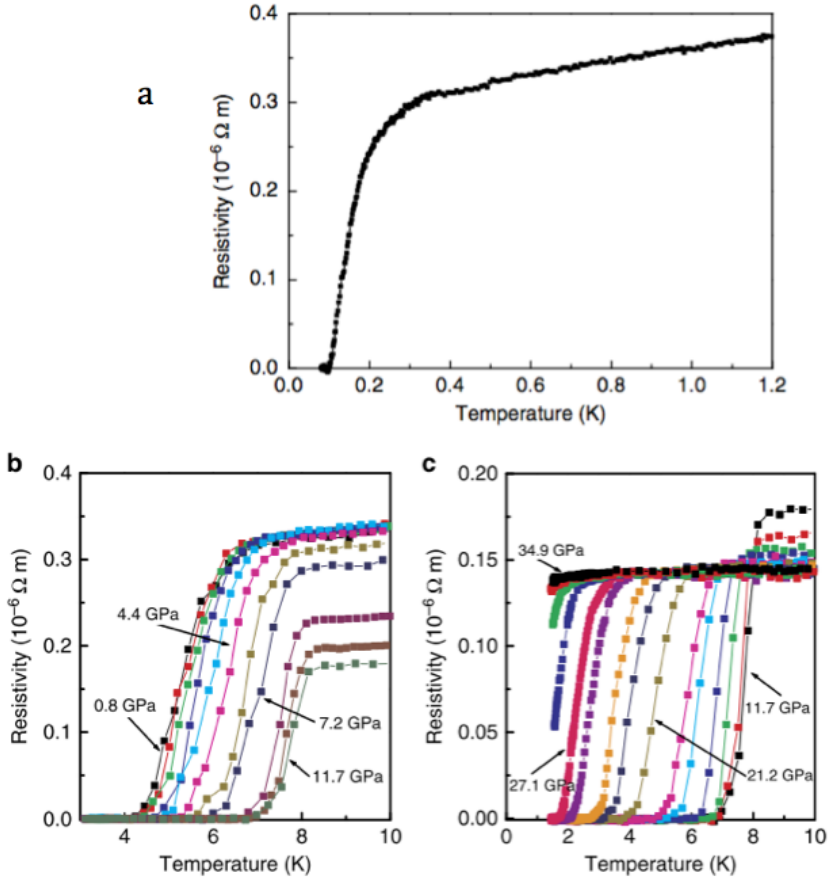

Figure 6: Evidence for superconductivity in 1T'-$MoTe_2$ at ambient pressure (a), at pressures ranging from 0.8 GPa to 11.7 GPa (b) and at pressures ranging from 11.7 GPa to 34.9 GPa, from [4]. Those results indicate a maximum temperature transition to the superconducting state at 8.2 K for 11.7 GPa (c).

that the electron's mass does not change, Newton's second law of motion gives:

$$m\frac{d\mathbf{v}}{dt} = -e\mathbf{E} - e\mathbf{v}\times\mathbf{B} - \frac{m}{\tau}\mathbf{v} \tag{1}$$

where e is the elementary charge in Coulomb (C) and τ is the inverse probability per unit time an electron experiences a scattering by the ions. The introduction of the cyclotron frequency $\omega_c = \frac{e\mathbf{B}}{m}$, and the multiplication by $-ne$ where n is the number of charge carriers per unit volume, yields for the current density $\mathbf{j}$.

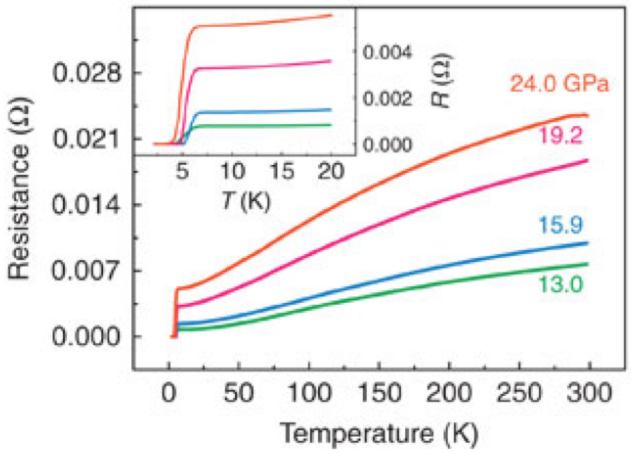

Figure 7: Evidence for superconductivity in 1T'-WTe_2 at pressures ranging from 13 to 24 GPa, taken by [9]

$$\frac{d\mathbf{j}}{dt} = \omega_c \times \mathbf{j} - \frac{\mathbf{j}}{\tau} + \frac{ne^2}{m}\mathbf{E} \tag{2}$$

An application of the Drude model without magnetic field gives the following value for the conductivity: $\sigma = \frac{ne^2\tau}{m}$. With this, and in steady state conditions, equation 2 becomes:

$$\mathbf{E} = \frac{\mathbf{j}}{\sigma} - \frac{\tau}{\sigma}\omega_c \times \mathbf{j} \tag{3}$$

The projection of equation 3 on the x and y axis gives in matrix form:

$$\mathbf{E} = \frac{1}{\sigma}\begin{pmatrix} 1 & \omega_c\tau \\ -\omega_c\tau & 1 \end{pmatrix}\mathbf{j} = \underline{\underline{\rho}} \cdot \mathbf{j} \tag{4}$$

where $\underline{\underline{\rho}}$ denotes a 2 x 2 matrix. In steady state conditions, when the transverse field E_y balances exactly the Lorentz force, one can assume that the transverse current j_y is 0. We define the magnetoresistance (MR) δ as:

$$\delta = \frac{\rho_{xx}(B) - \rho_{xx}(0)}{\rho_{xx}(0)} \tag{5}$$

With this simple model, there is no dependence of the MR with the magnetic field. Also the less naive semiclassical model gives a similar result, provided the electrons move in closed

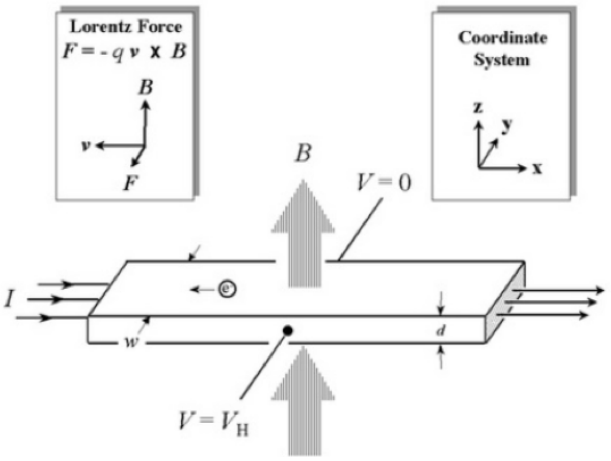

Figure 8: Classical Hall effect, as described by the NIST (National Institute for Standards and Technology)

orbits and the relaxation time τ is sufficiently large so that the orbits can be traversed many times between successive collisions (ref [10]):

$$\lim_{\frac{\tau}{T}\to\infty} \mathbf{j}_\perp = -\frac{n_{eff}ec}{B}\ \mathbf{E}\times\mathbf{B} \tag{6}$$

where $\mathbf{j}_\perp$ is the current of the electrons perpendicular to the magnetic field, n_{eff} is the total density of electrons minus the total density of holes and T is the period of time needed for the electron to go around the orbit. Here again, the magnetoresistance does not depend on the magnetic field. However, this model is only verified in some metals, and experiments have shown drastic deviations from it. For example WTe_2, Ali *et al.* found an increase of resistance of 452,000 % at 4.5 K with a magnetic field of 14.7 T, and an increase of 13,000,000 % at 0.53 K when the magnetic field is equal to 60 T, as shown in figure 9 [3]. In the Td phase of $MoTe_2$, Qi *et al.* also observed a change in resistivity due to the applied magnetic field (see the supplementary material of reference [4]). The longitudinal MR reached 10^5 % at 1.4 K without any sign of saturation up to 66 T.

A finer model would consider several bands that are partially filled. In this configuration, we can write, for each unfilled band n, $\mathbf{E} = \underline{\underline{\rho_n}} \cdot \mathbf{j}_n$, with

$$\underline{\underline{\rho_n}} = \begin{pmatrix} r_n & -R_nB \\ R_nB & r_n \end{pmatrix} \tag{7}$$

with R_n the Hall coefficient and r_n the longitudinal resistance. Then the relationship

between the electric field and the total current is $\mathbf{E} = \underline{\underline{\rho}} \cdot \mathbf{j}$, with:

$$\underline{\underline{\rho}} = (\sum_{n \in \, unfilled \; bands} (\underline{\underline{\rho_n}})^{-1})^{-1} \tag{8}$$

For a two-band model the expression of the total longitudinal resistance r is given by:

$$r = \frac{r_1 r_2 (r_1 + r_2) + B^2 (R_2^2 r_1 + R_1^2 r_2)}{(r_1 + r_2)^2 + B^2 (R_1 + R_2)} \tag{9}$$

If the material is perfectly compensated, that is to say if there is the same number of positive and negative charge carriers, then $R_1 + R_2 = 0$ and r shows a quadratic dependence with the magnetic field $\mathbf{B}$. Sondheimer *et al.* [11] found an expression for the longitudinal resistance directly in terms of mobility μ and charge carrier density n and p for electrons and holes, respectively:

$$\rho_{xx} = \frac{(n\mu_e + p\mu_h) + (n\mu_e \mu_h^2 + p\mu_e^2 \mu_h) B^2}{e[(n\mu_e + p_m u_h)^2 + (p-n)^2 \mu_e^2 \mu_h^2 B^2]} \tag{10}$$

where the subscript e stands for the electron band and the subscript h stands for the hole band. As a result, the MR δ has the following expression:

$$\delta = \frac{\rho_{xx}(B) - \rho_{xx}(0)}{\rho_{xx}(0)} = \frac{(n\mu_e + \mu_h)^2 + \mu_e \mu_h (n\mu_e + p\mu_h)(p\mu_e + n\mu_h) B^2}{(n\mu_e + p\mu_h)^2 + (p-n)^2 \mu_e^2 \mu_h^2 B^2} - 1 \tag{11}$$

If there is a compensation between the positive and negative charge carriers, then $p \approx n$, and as long as $(p-n)^2 \mu_e^2 \mu_h^2 B^2 \ll (n\mu_e + p\mu_h)^2$, the first term in the denominator can be neglected and the MR can be approximated by:

$$\delta = \frac{\Delta\rho}{\rho} = \mu_e \mu_h B^2 \tag{12}$$

It is noticeable that the large MR disappears with increasing temperature and with increasing pressure [9]. This two-band model has been fitted to match the experimental data [12], as displayed in figure 9(b). This seems to indicate that the two-band model is appropriate to describe the electronic properties of WTe_2.

Quantum oscillations Quantum oscillations are visible when one measures the electronic properties of a material such as the Hall resistivity, the longitudinal resistance or the Seebeck coefficient. Their study enables one to find the dimensionality of this material as well as its carrier density. In other words, analyzing the quantum oscillations of WTe_2 and $MoTe_2$ would enable a verification of WTe_2 and $MoTe_2$'s carrier compensation.

Zhu *et al.* [13] collected the Seebeck's response of WTe_2 under three orientations of the magnetic field along the high-symmetry axes and extracted the frequency of the resulting

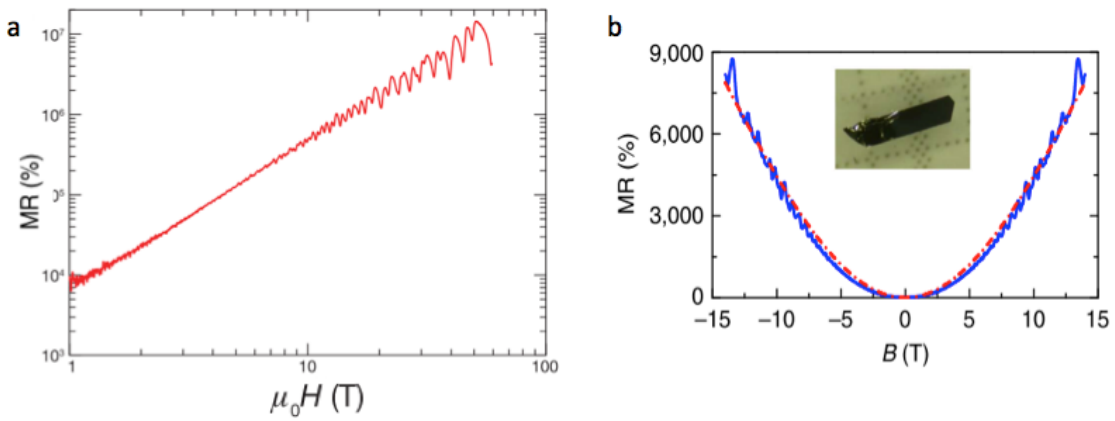

Figure 9: Ali *et al.*[3] observed a large, non saturating magnetoresistance in the bulk of WTe_2 at up to 60 T and at 0.53 K, with I parallel to a and H parallel to c. The dependance was found to depend quadratically on the applied magnetic field (a). This dependence was then confirmed by Wang *et al.* and fitted with a two-band model for a semimetal (b). Here the blue curve displays the experimental data, the red dashed-dotted line the theoretical fit and the inset shows a picture of a WTe_2 sample, from [12].

quantum oscillations. The Onsager relation $F = \frac{\hbar}{2\pi e} \cdot A_k$ links F, the extracted frequency, with A_k, the extremal cross section of the Fermi surface. In the case of WTe_2, it is possible to approximate the pockets as triaxial ellipsoids, and electronic structure calculations help deducing their hole or electron character. The Fermi surface was found to be composed of two pairs of electron like and hole like pockets (symmetric with respect to the Γ point), one electron (hole) pocket enclosing the other electron (hole) pocket. Because, from these measurements, a frequency could be extracted for each of the three high-symmetry axes and for each pocket, the electronic structure of WTe_2 should be tridimensional.

The resulting carrier concentration was $n = 6.64 \cdot 10^{19}$ cm^{-3} for the electrons and $p = 6.9 \cdot 10^{19}$ cm^{-3} for the holes, giving a precision for the compensation of $\approx 4\%$.

2 Weyl semimetals in condensed matter

2.1 Basic concepts for the study of topological materials

Just like graphene enabled the study of the Dirac fermion, the study of WTe_2 and $MoTe_2$ band structure's topology led to the investigation of a new particle: the type II Weyl fermion. In this section, I follow reference [14] and I present the concepts that are necessary to understand the interest in topological materials as well as the tools to investigate them

experimentally.

Definitions

The Berry phase In Condensed Matter physics, the Berry phase is used to see the evolution of the eigenstates as we vary the parameters such as the magnetic field or the strain. We consider $|n(R)\rangle$, an eigenstate of $H(R)$ such that :

$$H(R)|n(R)\rangle = E_n(R)|n(R)\rangle \tag{13}$$

The parameters need to vary adiabatically with time, that is to say their variation need to be small relative to the energies we are interested in (the gaps in the band structure). With the adiabatic theorem, once a system is prepared in an initial pure state $|n(R(0))\rangle$, this system will evolve with $H(R)$ and will stay as an instantaneous eigenstate of the Hamiltonian $H(R(t))$ throughout the process.

Hence, using the Schrödinger equation, we look at the time evolution of a wave function $|\phi(t)\rangle = e^{-i\theta(t)}|n(R(t))\rangle$, $\theta(t)$ being the phase of the state $|n(R)\rangle$ at time t. The parameters are supposed to vary adiabatically along a closed path $\mathcal{C}$ in parameter space, which we consider to be in 3 dimensions: $\mathbf{R} = (R_1, R_2, R_3)$. In our case, this parameter space will be the momentum space and we assume that the phase is smooth and single valued along this contour.

$$H(R(t))|\phi(t)\rangle = i\hbar\frac{d}{dt}(|\phi(t)\rangle) \tag{14}$$

which results into the following differential equation:

$$E_n(R(t))|n(R(t))\rangle = \hbar\frac{d\theta}{dt}n(R(t))\rangle + i\hbar\frac{d}{dt}(n(R(t))\rangle) \tag{15}$$

Multiplying by $\langle n(R(t))|$ and assuming that the state is normalized, one gets

$$\frac{d\theta}{dt} = \frac{E_n}{\hbar} - i\langle n(R(t))|\frac{d}{dt}|n(R(t))\rangle \tag{16}$$

which allows us to separate the phase evolution into two parts: a dynamical phase, linked to the energy evolution of the eigenstate, and a Berry phase γ_n, linked to the evolution of the eigenstates themselves.

$$\theta(t) = \frac{1}{\hbar}\int_0^t E_n(R(t'))dt' - i\int_0^t \langle n(R(t'))|\frac{d}{dt'}|n(R(t'))\rangle dt' \tag{17}$$

Since we are interested in the evolution of the eigenstates with the parameters and not with time, we can redefine the Berry phase as:

$$\gamma_n = i\int_{\mathcal{C}}\langle n(R)|\nabla_R|n(R)\rangle dR \tag{18}$$

where $\mathcal{C}$ is the closed contour in parameter space defined previously.

It is noticeable that the Berry phase has to be imaginary, otherwise it would not be a phase. As such, we can keep only the imaginary part in the previous expression: As this phase is defined over a 1D manifold (a curve), this concept will be relevant in a 1D insulator or in the 1D Fermi surface of a 2D metal.

The Berry vector potential We introduce here $A_n(R) = i\langle n(R)|\nabla_R|n(R)\rangle$, the Berry vector potential. With this, the Berry phase is defined as:

$$\gamma_n = i\int_{\mathcal{C}} A_n(R)dR \tag{19}$$

This Berry potential built from the electron's wave functions is the equivalent of the magnetic field in momentum space.

The Berry curvature Stokes theorem allows us to introduce the Berry curvature and calculate the Berry phase as the flux of this curvature through the area bonded by the contour $\mathcal{C}$ in parameter space:

$$\gamma_n = -\mathrm{Im}(\int_{\mathcal{C}} d\mathbf{S}\cdot(\nabla\times\langle\nabla n(R)|\nabla|n(R)\rangle)) \tag{20}$$

The Berry curvature is given by $\mathrm{Im}(\nabla\times\langle\nabla n(R)|\nabla|n(R)\rangle))$.

The use of the Berry phase or the Berry curvature depends on the dimensionality of the system and on whether the system is a metal or an insulator. We saw that the Berry phase was appropriate to describe a 1D insulator or the 1D Fermi surface of 2D metals. In contrast, the Berry field is integrated over two dimensions and will appropriately describe filled bands in two dimensions or the 2D Fermi surface of 3D metals. Thus, in the case of a semimetallic three dimensional electronic structure, which is the case for WTe_2 and for $MoTe_2$, the description of topological properties will involve the Berry field.

Derivation of a gauge independent Berry phase and Berry curvature For a closed path, the Berry phase is a gauge invariant quantity independent of the specific form of how $\mathbf{R}$ varies in time. In order to obtain a gauge independent computation for the Berry phase, relevant for the following calculations, one introduces a complete set of eigenstates at each $\mathbf{R}$, $\sum_m |m\rangle\langle m| = 1$ and removes the derivatives on the eigenstates, as explained in reference [14].

$$\gamma_n = -\int\int_{\mathcal{C}} d\mathbf{S}\cdot\mathrm{Im}\sum_{m\neq n}\frac{\langle n(\mathbf{R})|\nabla_R(H(\mathbf{R}))|m(\mathbf{R})\rangle\times\langle m(\mathbf{R})|\nabla_R(H(\mathbf{R}))|n(\mathbf{R})\rangle}{(E_m(\mathbf{R})-E_n(\mathbf{R}))^2} \tag{21}$$

Equation 21 does not depend on the phases of $|n\rangle$.

This derivation enables us to interpret the Berry curvature as the result of the adiabatic interaction of the level $|n\rangle$ with the other levels $|m\rangle$. In the expression 21, one introduces as well a new expression for the Berry curvature:

$$\mathbf{V}_n = \sum_{m \neq n} \frac{\langle n(\mathbf{R})|\nabla_R(H(\mathbf{R}))|m(\mathbf{R})\rangle \times \langle m(\mathbf{R})|\nabla_R(H(\mathbf{R}))|n(\mathbf{R})\rangle}{(E_m(\mathbf{R}) - E_n(\mathbf{R}))^2} \tag{22}$$

This Berry field (just like the one defined equation 20) is integrated over a surface, and is thus relevant for filled bands in two dimensions (insulators) or for the 2D Fermi surface in three dimensional metals, both characterized by a Chern number. This is why, in the following section, I will refer more to the properties of the Berry curvature. However, this derivation is only valid when the energy level we consider is singly degenerate. In the case of a d-degenerate level, the Berry vector potential becomes a matrix of dimension d.

One can already guess the effect of a degeneracy by approaching the energy of the state m to the energy of the state n. Then, the denominator of equation 21 would be approaching zero and the Berry phase would not be defined in the corresponding point in parameter space, and would be considered as a monopole. Let us consider a two level system given by the following Hamiltonian:

$$H = \epsilon(\mathbf{R}) I_{2\times 2} + \mathbf{d}(\mathbf{R}) \cdot \sigma \tag{23}$$

where $\mathbf{d}(\mathbf{R})$ is a 3D vector that depends on the coordinates $\mathbf{R}$ and σ are the Pauli matrices. By neglecting the first term without restricting the generality, one finds the following energies for the eigenstates: $E_\pm = \pm\frac{\sqrt{\mathbf{d}\cdot\mathbf{d}}}{2}$.

The characterization of this two level system using both the Berry curvature and the Hamiltonian approach gives, for each eigenstate, a Berry field strength that has the form of a field generated by a monopole in $\mathbf{R}$-parameter space of strength $\frac{1}{2}$, as shown by Bernevig [14].

$$\mathbf{V}_\pm = \pm\frac{1}{2}\frac{\mathbf{d}}{d^3} \tag{24}$$

More generally, degeneracy points in parameter space act as sources and sinks of the Berry curvature, depending on the eigenstate. The sign in front of the field gives the topological charge of the degeneracy point.

Chern number and Hall conductance The Hall conductivity σ_H manifests itself in the off-diagonal current response:

$$j_i = \sigma_H \epsilon_{ij} E_j \tag{25}$$

where ϵ is the dielectric constant of the system. This quantity is quantized and is given by some integer of $\frac{e^2}{h}$. The Hall conductance is a true topological quantity as small adiabatic

transformations of the Hamiltonian do not change it and it does not depend on the energies of the occupied bands, but only on the eigenstates. An insulator can be adiabatically interpolated from a two level system, with an occupied ground state and an empty excited state, such that no band cross the Fermi level (the eigenvalues remain gapped) and the structure of the band energies remains the same. The resulting Hamiltonian will be topologically equivalent to the first one. The analysis of the linear response of an insulator to the application of an electric and magnetic field gives an expression of the Hall conductance of a 2D system as the integral of the Berry curvature over the full BZ:

For a filled band, the Hall conductance will be an integer called the Chern number, given by equation 26.

$$\sigma_{xy}^{Hall} = \frac{e^2}{h}\frac{1}{(2\pi)}\int\int dk_x dk_y F_{xy}(\mathbf{k}) \tag{26}$$

where σ_{xy}^{Hall} is the Hall conductivity of a band insulator whose Fermi level is in the gap and F_{xy} is the Berry curvature given by

$$F_{xy}(\mathbf{k}) = \frac{\delta A_y(\mathbf{k})}{\delta k_x} - \frac{\delta A_x(\mathbf{k})}{\delta k_y} \tag{27}$$

We recall that $\mathbf{A}$ denotes the Berry vector potential. For a single band, this quantity is an integer called a Chern number. The total Chern number, defined as the sum of the Chern numbers of all occupied bands, should remain invariant under gauge transformation, provided the gap separating occupied and empty bands remains finite. Because of the open boundary conditions, the Chern number should be zero unless we cannot pick a gauge that leaves the Berry potential well defined. In other words, a non zero Chern number implies a degeneracy in the Berry curvature at points in $\mathbf{k}$-space where the smooth gauge used for the rest of the BZ has to be changed. The $\mathbf{k}$-points where the phase convention is different are referred to as Weyl points in Weyl semi-metals, as described figure 10. The Chern number is the winding number of the gauge transformation at the boundary where the definitions of the wave function have to be changed. This is why this number is an integer, and it is used to characterize gapped band structures and to classify them.

In 1988, Haldane proposed a lattice model to show that materials that have a non trivial topological band structure characterized by a non-zero Chern number could exhibit a quantum Hall effect even without the presence of a magnetic field. The non-zero conductance in an insulator indicates that, even if the bulk is gapped, the system somehow transports electrons. This means that there must be surface states ready to receive or donate electrons. If two insulating materials with a different Hall conductance are put close to one another along a boundary that respects the bulk insulating state, then the bulk gap has to collapse and reopen again somewhere in the boundary region. In Chapter 8 of reference [14], Bernevig derives the wave function of a chiral propagating mode localized on the edge where the Hall conductance changes. This description is summarized in figure 11.

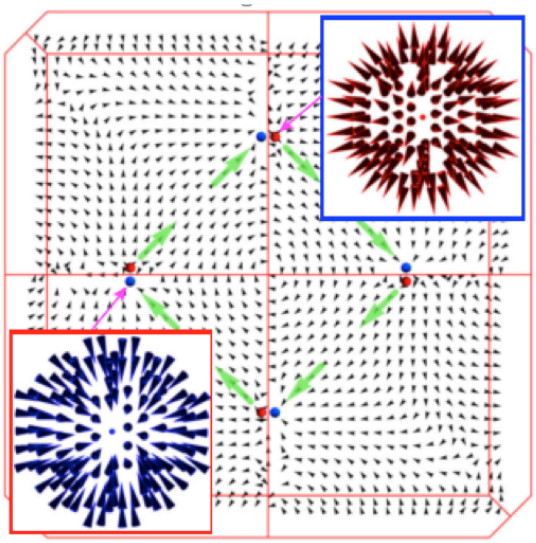

Figure 10: Distribution of the Berry curvature in the non-centrosymmetric tantalum monoarsenide TaAs whose structure lacks inversion symmetry for the $k_z = 0.592\ \pi$ plane, as calculated by [15]. The inset shows the hedgehoglike Berry curvature near the Weyl points: this is a consequence of the fact that the Berry potential is not well defined at these particular **k** points.

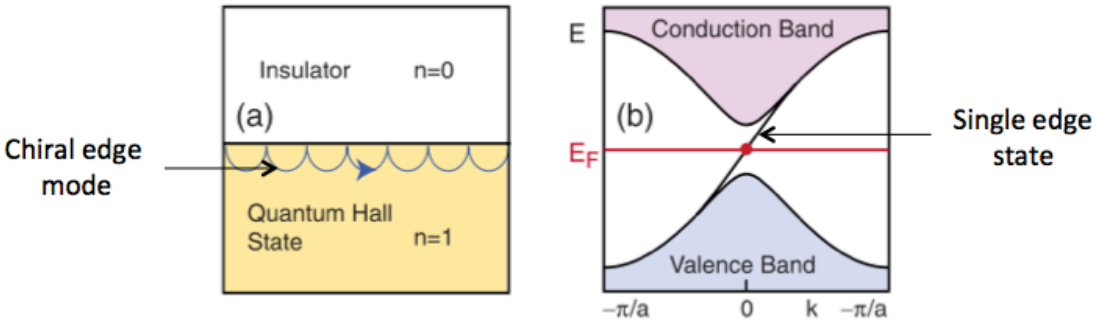

Figure 11: Existence of chiral states at the boundary between two environments with a different Chern number (a), from [16]. The single edge state is connecting the conduction band with the valence band: no states available for backscattering, so these states are insensitive to disorder (b)

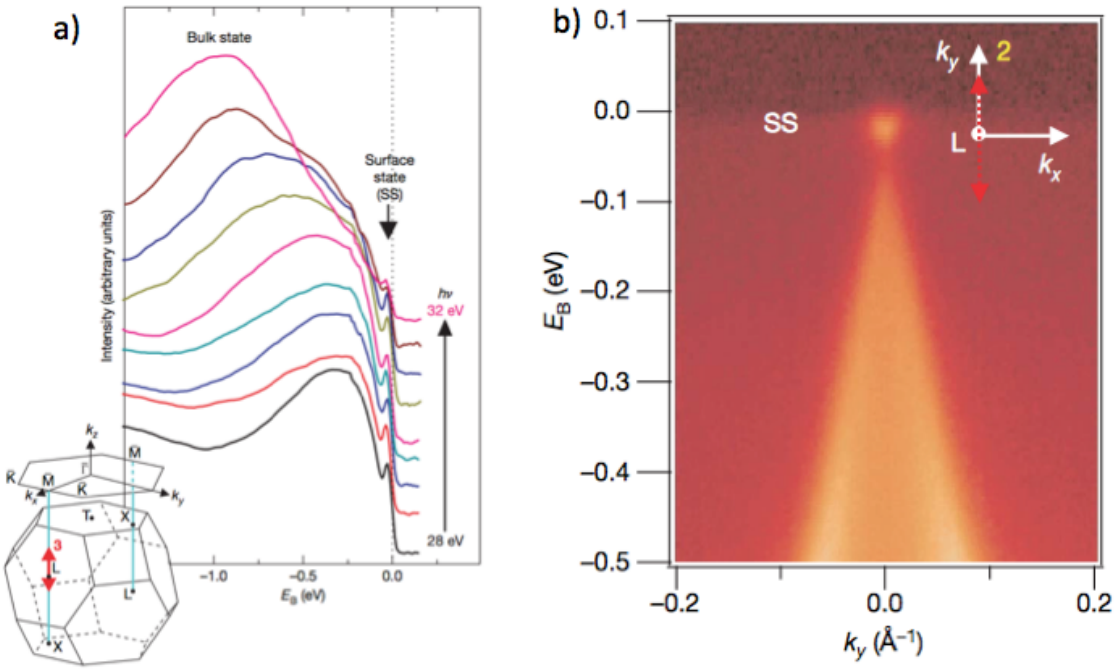

Figure 12: Evidence of a surface state in the bismuth-antimony alloy system (a). The dispersion cut of $Bi_{0.9}Sb_{0.1}$ near the L point of the bulk BZ is Dirac like (with a photon energy of 29 eV), from [17].

The first experimental evidence for a topological insulator was found in bismuth based materials in 2007, as shown figure 12 [17]. Those materials are band insulators in the bulk but feature spin-polarized Dirac electronic states on their surface.

Since then, there has been numerous discoveries of new topological phases of matter.

The Dirac equation and its solutions Dirac wanted to link the relativity and quantum mechanics. So originally, Dirac fermions were used in high energy physics to describe the motion of free relativistic fermions. This is why, before describing them in condensed matter, I provide here a brief summary on Dirac fermions and solutions of the Dirac equation. This will allow me to introduce Weyl fermions.

The Dirac equation is a relativistic field equation, so it respects the Lorentz invariance. We consider a field Φ and a differential operator $\mathcal{D}$. Saying that the equation $\mathcal{D}\Phi$ is Lorentz invariant means that, for a given field Φ satisfying the equation, if we transform it in a new frame of reference, it will satisfy the same equation [18]. This transformation can be a rotation of angle θ or a boost of velocity v.

$$(i\gamma^\mu \partial_\mu - m)\Phi = 0 \tag{28}$$

The Dirac matrices γ^μ need to respect the following relations in the Minkowski metric, so that $H^2 = \mathbf{p}^2 + m^2$, the Hamiltonian of a free particle of mass m with $\hbar = c = 1$, is not violated:

$$[\gamma^\mu; \gamma^\nu]_+ = 2g^{\mu\nu}\mathbb{I}_4 \tag{29}$$

$$\gamma^0\gamma^\mu\gamma^{0\dagger} = \gamma^{\mu\dagger} \tag{30}$$

$$\gamma^{0\dagger} = \gamma^0 \tag{31}$$

$$\gamma^\mu = -\gamma^{\mu\dagger} \tag{32}$$

where $g^{\mu\nu}$ is a 4 x 4 matrix used in the Minkowski metric and is given by $g^{\mu\nu}$ = diag(1,-1,-1,-1) and the g^μ, where $\mu \in \{0, 1, 2, 3\}$ are a set of four 4 x 4 matrices that satisfy the equations 29, 30, 31 and 32. So the Dirac equation is actually a set of four equations and the Dirac spinor (complex vector) has four components.

A set of matrices that verify these relations is given by:

$$\gamma^0 = \begin{pmatrix} 0 & 1 \\ 1 & 0 \end{pmatrix} \quad \gamma^i = \begin{pmatrix} 0 & \sigma^i \\ -\sigma^i & 0 \end{pmatrix} \tag{33}$$

where the σ^i are the Pauli matrices [18].

Note that if there are two choices of Dirac matrices that respect 29 and 30, then they are related by a unitary matrix. The different solutions of the Dirac equation depend on the condition imposed on the fermion field $\Phi(x)$. Majorana fermions are their own antiparticle whereas the solution proposed by Weyl enables fermions that have unambiguously a left or right chirality by being massless and projected onto the right or left chiral projection of the Dirac field.

Weyl fermions Let us first consider the helicity and the chirality of Dirac fermions, following reference [19].

The helicity of a fermion is defined by the relative orientation of its momentum $\mathbf{p}$ and its angular momentum $\mathbf{J}$:

$$h_p = \frac{2\mathbf{J} \cdot \mathbf{p}}{|\mathbf{p}|}$$

For a Dirac fermion, the eigenvalues are +1 for right helical fermions and -1 for left helical fermions. Since it commutes with the Dirac Hamiltonian, it does not change with time. But for a massive fermion, the observer can move faster than the particle along the same direction, which would reverse the sign of helicity. Thus, by definition of the Lorentz invariance, helicity is not Lorentz invariant. However, when the fermion is massless, it moves at the speed of light so the helicity becomes Lorentz invariant.

We define the chirality of a particle by taking its left and right chiral projection defined by:

$$L = \frac{1}{2}(1 - \gamma^5)$$
$$R = \frac{1}{2}(1 + \gamma^5)$$

where γ^5 is a matrix that anticommutes with all Dirac matrices and is defined by $\gamma^5 = i\gamma^0\gamma^1\gamma^2\gamma^3$. The chirality of the solution of a Dirac equation is conserved under Lorentz transformation but is not conserved over time because γ^5 does not commute with the mass term of the Dirac Hamiltonian. This mass term represents in fact the coupling between the right chiral and the left chiral part of the Dirac fermion.

Since Weyl fermions are already projected onto the left chiral or right chiral space of the Dirac field, and since the fact that they are massless ensures that the chirality is conserved over time, defining them by their chirality (or by their helicity) makes sense. The two component spinor describes right moving or left moving fermions.

In fact, this decomposition into left chiral fermions and right chiral fermions is so powerful that Weyl fermions are used as building blocks of any general fermion field. Following reference [18], in terms of Φ_L and Φ_R, where Φ_L is the left handed and Φ_R the right handed spinor, the Dirac equation can be rewritten as:

$$(i\gamma^\mu\partial_\mu - m) = \begin{pmatrix} -m & i(\partial_0 + \sigma \cdot \nabla) \\ i(\partial_0 - \sigma \cdot \nabla) & -m \end{pmatrix} \begin{pmatrix} \Phi_L \\ \Phi_R \end{pmatrix} = 0. \tag{34}$$

The mass term couples Φ_L and Φ_R. Having $m = 0$ leads to two decoupled equations called Weyl equations.

The discovery of the Dirac fermion and of the Weyl fermion in Condensed Matter Semi-metals are metals with a vanishingly small density of states (DOS) at the Fermi level.The carrier concentration is often several orders of magnitude lower than the 10^{22}cm^{-3} typical of ordinary metals (except in $MoTe_2$). As an example, graphite has a carrier density of $3 \cdot 10^{18}\text{cm}^{-3}$. Despite the reduced DOS, low energy excitations are always present in a semimetal, which makes their study fundamentally different from the study of topological insulators.

Dirac semimetals In a Dirac semimetal, four bands cross linearly near the Fermi level, leading to an effective Hamiltonian given by:

$$H(\mathbf{k}) = \sum_i d_i(\mathbf{k})\sigma_i \tag{35}$$

where $i \in \{x, y, z\}$ is the indice of the Pauli matrices. We can set $d_x = k_x$ and $d_y = k_y$ without restricting the generality. If $d_z = 0$, then the fermion is gapless, whereas if not,

the Dirac fermion becomes massive and the Hamiltonian is gapped. We can write $d_3 = M$ where $M \neq 0$.

This Hamiltonian looks just like the two-level system described previously in equation 23. We have seen that, in this case, the Berry field strength has the form of a monopole in momentum space. As a result, the wave function of a Dirac fermion that is transported around a path $\mathcal{C}$ in momentum space will acquire a Berry phase.

Note that Dirac fermions can be massless or massive. Dibismuth triselenide (Bi_2Se_3) is a three-dimensional topological insulator that has a linearly dispersed Dirac surface state (13(a), (b) and (c)). The introduction of Fe dopants in the bulk induces magnetic order which breaks time reversal symmetry [20]. A system respects time-reversal symmetry when the particles retrace their motion when the arrow of time is reversed. This breaking of time-reversal symmetry induces a gap: the bands do not disperse linearly around the Dirac point. To create the massive Dirac fermion state, the Fermi level needs additionally to lie between the upper and lower part of the surface Dirac cone. This is achieved by using Manganese (Mn) that simultaneously maintains the magnetic doping effect and p-dopes the samples.

Weyl semimetals If we consider a Hamiltonian with N discrete energy eigenvalues determined by:

$$\sum_{\ell=1}^{N} H_{j\ell}(\mathbf{k})\phi_{\ell}^{(i)}(\mathbf{k}) = \omega_i \phi_j(\mathbf{k}) \tag{36}$$

with $i \in [\![1; N]\!]$. We consider the case where the i^{th} and $(i+1)^{th}$ levels are degenerate in the dispersion space $(E_d(\mathbf{k}), k_d)$. Following reference [21], we expand $H(\mathbf{k})$ around this degeneracy point and limit ourselves to the first order. Using the 2 x 2 submatrix formed by the i^{th} and $(i+1)^{th}$ entries of the expanded matrix, after changing variables, we can have an eigenvalue equation for the i^{th} and $(i+1)^{th}$ energy eigenvalues around E_d given by:

$$\mathbf{k}\sigma\mathbf{u} = \pm k^0 \mathbf{u} \tag{37}$$

with $\mathbf{u}$ the eigenvectors and k^0 the eigenvalues of the Hamiltonian. We call the points in momentum space where this degeneracy occurs $(E_d(\mathbf{k}), k_d)$ the Weyl nodes, and there, Berry curvature is not well defined, as described in figure 10. Around these nodes, the energy levels are well described by the right-handed or left-handed Weyl equation: Weyl fermions, present in a Weyl semi-metal, are massless and have a defined chirality.

Since this topological charge has to disappear over the whole BZ, these nodes have to appear in multiples of two (Weyl fermion doubling theorem). If, in addition, the Hamiltonian of the system is invariant under time-reversal (TR) symmetry, for each monopole, an anti-monopole of the same charge for the opposite k-vector exists, due to the symmetry of the Berry field. Finally, since an anti-monopole has to compensate for each monopole, Weyl nodes should appear in multiples of four when the system is invariant under TR.

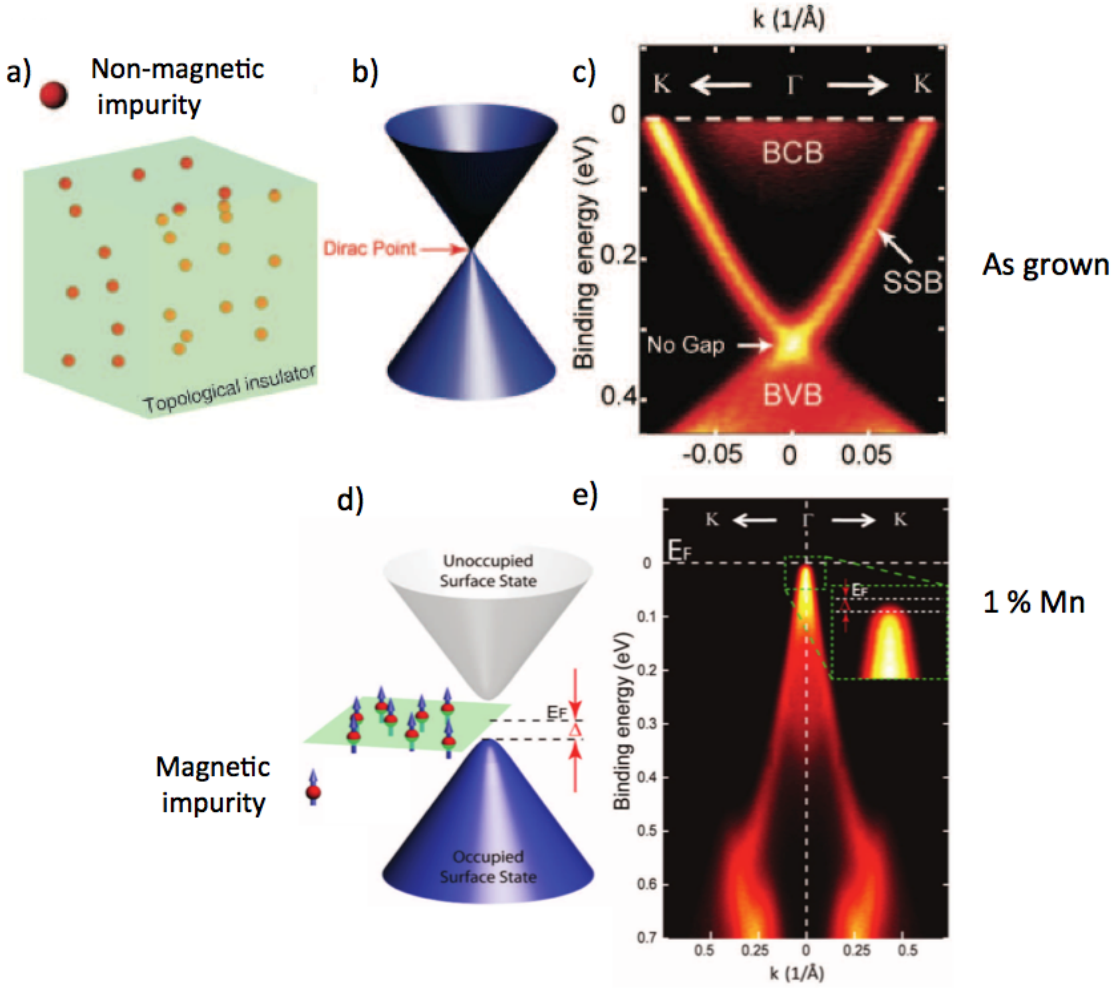

Figure 13: Massless and massive Dirac points probed with ARPES. Bi_2Se_3 is topological insulator. When it is undoped magnetically, the bulk valence band (BVB) connects the surface state band (SSB) at the Dirac point (panel (b) and (c)). The presence of the bulk conduction band (BCB) indicates that the Fermi energy does not lie inside the gap. Doping magnetically this compound with Manganese ($Bi_{0.99}Mn_{0.01}Se_3$, panels (d) and (e)) positions the chemical potential inside the gap and breaks the Dirac point, which results in a massive Dirac fermion state, from [20]. Δ is the energy difference between the chemical potential and the top of the Dirac cone.

Due to their topological character, Weyl fermions should be robust against any perturbation that preserves translational symmetry as it would only move the Weyl nodes**k** space. Small perturbation cannot make a Weyl node disappear: only a monopole and antimonopole can annihilate each other. Generally Weyl points are far away from each other, so making a monopole and an antimonopole of the Berry curvature meet would require large changes in the Hamiltonian.

Type I Weyl semimetals An alternative expression to describe the Weyl points is given by the following Hamiltonian:

$$H(\mathbf{k}) = k_i A_{ij} \sigma_j \tag{38}$$

where A_{ij} is a 3 x 4 matrix (where $i \in \{x, y, z\}$ and $j \in \{0, x, y, z\}$ is the indice of the 2 x 2 unit and Pauli matrices [22]). Each degeneracy point in (E($\mathbf{k}$), $\mathbf{k}$) space corresponds to a specie of Weyl fermion. In the type I Weyl semi-metals, the effect of the A_{i0} is negligible compared to the effect of the A_{ij} with $j \in \{x, y, z\}$. As a result, the crossing of the two bands forms a cone that can cross the Fermi level at a singular point such that the energy map at this energy is points like. In fact, the whole bulk Fermi surface can only consist of a set of momentum points and their corresponding surface states.

Type II Weyl semimetals

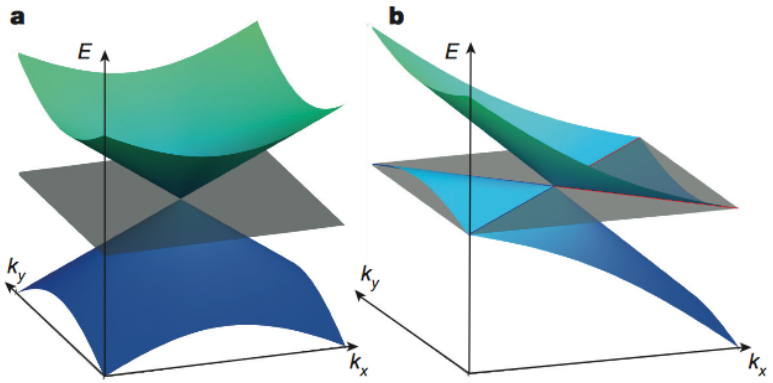

Figure 14: The difference between type I and type II Weyl semimetals: type II break the Lorentz invariance, from [22].

The study of 1T'-WTe_2's and 1T'-$MoTe_2$'s band structure topology lead to the first theoretical prediction of type II Weyl semimetals. They are actually described by the same equation 38, except that the A_{i0}, corresponding to the part of the energy spectrum linear in momentum, have a dramatic effect on the Weyl node. To highlight this difference, we rewrite equation 38:

$$H(\mathbf{k}) = k_i \nu_i + k_i A_{ij} \sigma_j \tag{39}$$

where $j \in \{x, y, z\}$.

The left term, $k_i \nu_i$, is a linear term that is of the same order as the Weyl term $k_i A_{ij} \sigma_j$. If this term becomes dominant over the other one in a certain direction in momentum space, then the cone-like spectrum is tilted, as shown in figure 14. This results in the touching of the electron and hole pocket, and the Fermi surface cannot be point-like for type II Weyl semi-metals. The fermions that can be described by this equation are still Weyl points in the sense that they are massless and can still be assigned one chirality, but the left term breaks the Lorentz invariance.

2.2 Experimental signatures of a Weyl semimetal state

2.2.1 Arc-like Fermi surface

For simplicity, we consider here a type I Weyl semimetal.

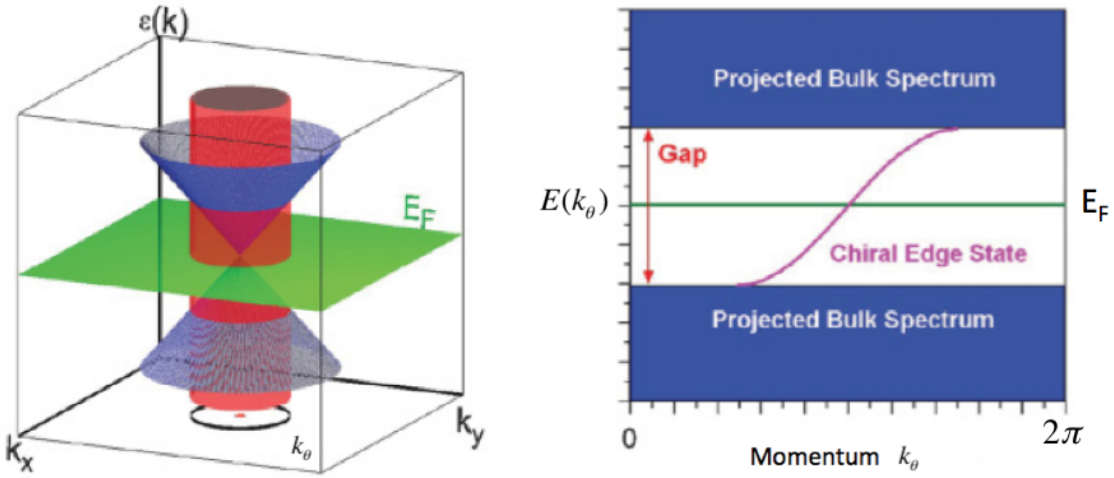

Figure 15: Band dispersion near a Weyl node with respect to (k_x, k_y), the bulk states fill the inside of the cone (on the left) The red cylinder defines a one-dimensional circular dispersion, from [23]. In the band structure of the 2D-subsystem (on the right), the upper states have a different Hall conductance than the lower states, resulting in the appearance of a surface state crossing the Fermi level.

In figure 15, the red cylinder with radius R enclosing the Weyl point is the basis for a one-dimensional Fermi surface. The dispersion plot giving the energy dispersion with respect to $k_\theta = R \cdot cos(\theta) + R \cdot sin(\theta)$ displays the band structure of this red cylinder unrolled onto a plane, as shown on the right side of figure 15. Since a Weyl node corresponds to a crossing of bands, the upper projected bulk spectrum has a different Chern number than

the lower projected bulk spectrum. This corresponds to a quantum Hall insulator. Hence, for each cylinder of radius R enclosing the Weyl node, there exist a state crossing the Fermi level at $k = k_R$, as long as the Chern number of the upper projected bulk spectrum is different than the one of the lower projected bulk spectrum. In other words, as soon as the cylinder is large enough to enclose two Weyl points of opposite chirality, there is no edge state linking the upper projected bulk spectrum and the lower projected bulk spectrum that crosses the Fermi level. This results in the appearance of a Fermi arc linking the projection of two Weyl points of opposite chirality on the Fermi surface, as shown figure 16.

This provides another explanation for the necessity for Weyl nodes to appear in multiples of two. Each monopole of the Berry curvature has a string attached to it. But, unlike in high-energy physics, in condensed matter, there is a natural bandwidth cutoff that forces the string to end in another monopole.

Finally, a Fermi arc surface state is going from the source to the sink of the Berry curvature and suggests that the system transports electrons from one Weyl point to the other at the surface of the material. This behavior is different from the one in metals, where the Fermi surface always displays a closed contour. This arc is a surface state, and should thus be of 2D-character.

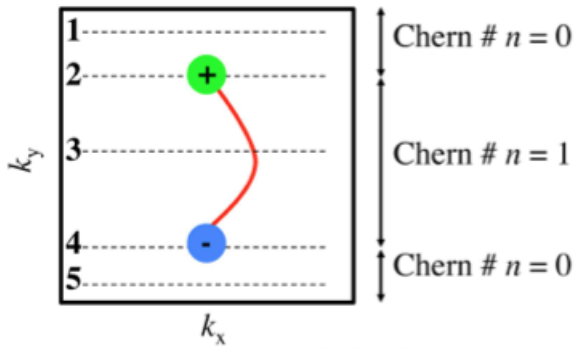

Figure 16: Fermi arcs arising from bulk Weyl points, from [24]. The surface state in the form of an arc is directly linked with the difference in the Chern numbers between and outside the Weyl nodes.

2.2.2 Chiral anomaly

Nielsen and Nimomiya demonstrated that the axial anomaly, derived from the production of Weyl particles and known as the Adler-Bell-Jackiw (ABJ) anomaly, could also exist in condensed matter [21]. This anomaly consists of the production of Weyl fermions when

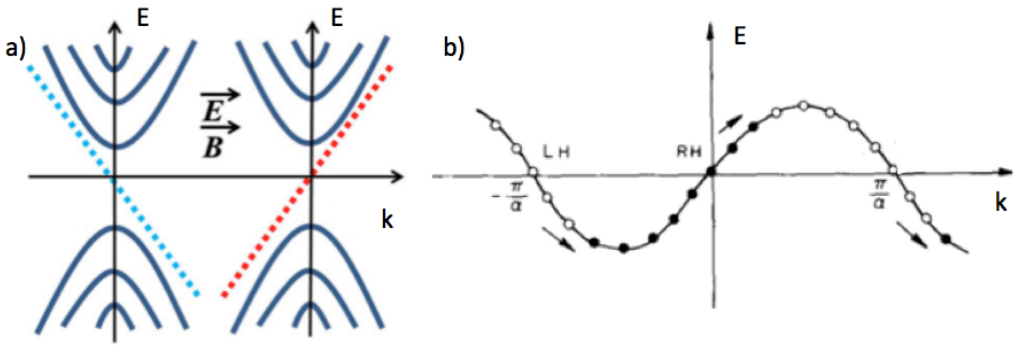

Figure 17: (a)Schematic description of the dispersion for the left-handed (left) and right-handed (right) Weyl fermion in the presence of parallel electric and magnetic fields [25]. The dotted lines represent the 0^{th} Landau levels. (b) Dispersion law for the right-handed Weyl equation. The arrow indicates the movement direction of the particles when the electric field is turned on, from [21]

external electric and magnetic fields are applied. By definition, Weyl fermions in condensed matter are low-energy excitations with a defined chirality.

When a magnetic field is applied, the energy levels of a right-handed of a left-handed Weyl fermion are given by the Landau levels, as displayed in the figure 17(a). For simplicity, we can consider the dispersion law in 1D of the right-handed fermion to be $E(k) = k$. The addition of an electric field $\mathbf{E}_{el}$ parallel to the magnetic field accelerates the electrons so that we can write : $\dot{E} = \dot{k} = eE_{el}$. Hence, the creation rate of right-handed particles in the Fermi surface equals to:

$$\dot{N_R} = L^{-1}\frac{L}{2\pi}\dot{E} = \frac{e}{2\pi}E_{el} \tag{40}$$

Similarly, the annihilation rate of the left-handed particles with dispersion law $E(k) = -k$ equal to:

$$\dot{N_L} = -\frac{e}{2\pi}E_{el} \tag{41}$$

Figure 17(b) represents the shift of particles when $\mathbf{E}_{el}$ is on along the dispersion law in 1D. There is a production of particles near $k = 0$ and an annihilation of the same amount of left-handed particles near $k = \frac{\pi}{a}$, a being the lattice constant. This is the chiral anomaly.

A consequence of this effect is a peculiar behavior of the electric current and a longitudinal magneto-conduction that becomes extremely strong. In $(E(\mathbf{k}), \mathbf{k})$ space, the left-handed and right-handed degeneracy points appear necessarily as a pair (Weyl fermion doubling theorem). We consider two cones described by the Weyl equation: the R cone is described by the right-handed Weyl equation whereas the L cone is described by the left-handed Weyl equation. Since there is an absence of net production of particles, they move from

the neighborhood of the L cone to that of the R cone. The excess electron produced by the ABJ anomaly in the R cone has to be scattered back to the states in the other cone, generating a anomalous current.

Because of the electron transfer towards the R cone, μ_R, the chemical potential for the electrons at the right-handed degeneracy point, increases, whereas μ_L, the left-handed one, decreases. Using the semiclassical Boltzmann equation, Son and Spivak showed the large momentum internode scattering resulted in the creation of an anomaly related contribution to the component of the conductivity tensor parallel to the applied magnetic field [26]. So the imbalance of electron populations due to the ABJ anomaly results in a finite current density which relaxes via intervalley scattering. When **E** is parallel to **B**, this may result in the observation of an anisotropic negative magnetoresistance. This phenomenon has indeed been observed in TaAs [25].

The new physical properties linked with this new state of matter can be revealed by determining accurately the Fermi surface and the dispersion near the Fermi level thanks to Angle Resolved Photoelectron Spectroscopy (ARPES). The experimental identification of new phases of matter in real materials enhances our understanding of the physics of topological matter. In particular, having an experimental proof of the type II Weyl semi-metal state is of fundamental importance, since it will provide a playground for the investigation of an anisotropic chiral anomaly and help understand the influence of interactions for Weyl fermions.

2.3 Prior experimental evidence for the Weyl semimetal state from ARPES

Type I Weyl semimetals Evidence of Weyl fermions in a material can be found either by revealing the Weyl nodes, or by showing a signature of these Weyl nodes, such as the arc-like surface states, as marked by the arrow in figure 18.

In principle, it is hard to differentiate a gapless band structure (Weyl node) from a band structure having a very small gap (of the order of 1 meV) using ARPES. This is why looking for arcs is the most straightforward method, provided these arcs are topological. Experimentally, one should combine the bulk band structure and the mapping of the surface Fermi arcs, which should link the projection of the Weyl nodes at the surface of the material [28]. Fermi arcs linking the projections of the Weyl nodes on the Fermi surface look like the ones found in the type I Weyl semimetal TaAs, shown in figure 18.

Type II Weyl semimetals For type II Weyl semimetals, in principle, one should look for the touching point of an electron and a hole pocket in a constant energy contour to locate the Weyl nodes. This seems to be the case for LaAlGe (see figure 19). From the Fermi surface and the dispersion plots, it is tempting to call this material a type II Weyl semimetal, however, the large energy scale and the linewidth of the dispersive bands in the experimental data, a small gap of a few meV cannot be excluded.

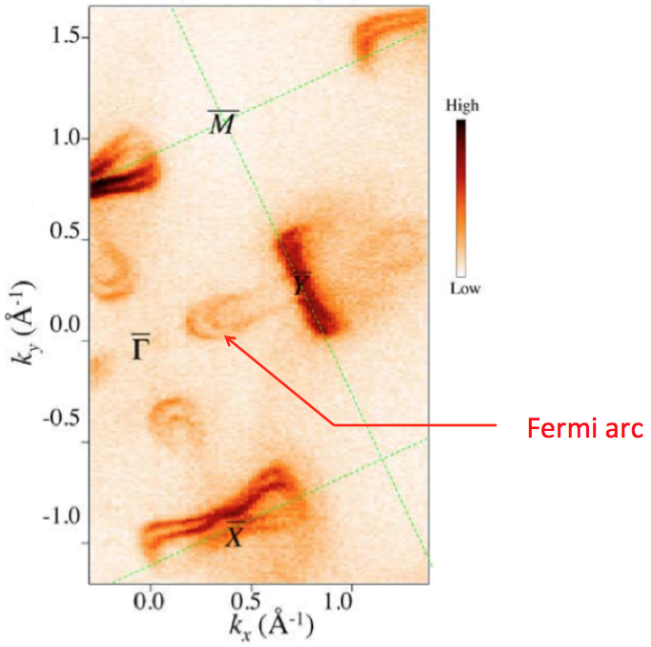

Figure 18: Fermi arcs appearing on the Weyl semimetal (001) surface TaAs, from [27]. The red arrow marks the Fermi arcs that are a consequence of the presence of the Weyl nodes.

In most cases, the Weyl nodes are not at the Fermi level, and this should be the case for both WTe_2 and $MoTe_2$ (see figure 21). In those cases, it is difficult to prove the type II Weyl semimetal state: we cannot see the touching point of the electron and hole pocket and, in addition, the arcs linking the Weyl nodes would most likely end inside a pocket. Type II Weyl semimetals also necessarily have a bulk Fermi surface. Not only does the presence of irrelevant bulk bands make the observation of Fermi arcs difficult to discern, the surface states relevant for our study can also hybridize with the bulk states. Since the Fermi arcs can end inside a pocket, when this is the case, there is no way of comparing its end with the supposed projection of the Weyl nodes onto the Fermi surface. In addition, because of the tilting of the cone, both Weyl nodes projection may lie in the same pocket: in that case, this arc is visible only if it emerges out of the pocket and the arc of those type II Weyl semimetals is not topologically protected. On the other hand, if the projection of the Weyl nodes end inside two distint pockets, then the surface state is still topologically protected.

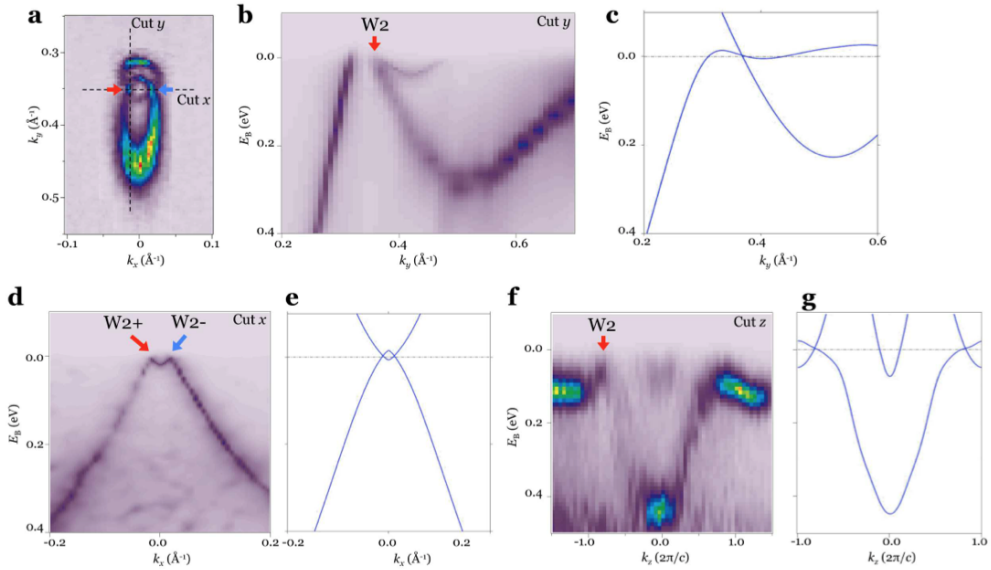

Figure 19: Experimental evidence for the crossing of an electron and hole pocket in the putative type II Weyl semimetal LaAlGe, from [29]. a) displays the Fermi surface where the electron and hole pocket cross. The energy dispersion plot parallel to ΓY in b) and its comparison with calculation provides a proof that the FS displayed in a) is indeed a crossing between the electron and hole pocket. This is the same thing for d) and e) parallel to ΓX and f) and g) parallel to ΓZ.

2.4 Electronic band structure and topological properties of WTe_2 and $MoTe_2$ from density functional theory

Density functional theory (DFT) is a standard technique to calculate the energy bands of solids. This method describes the electronic structure of solids in terms of quasi-independent particles filling up individual (Bloch) energy levels. In the case of WTe_2 and $MoTe_2$, the system is weakly interacting because the relevant orbitals (5s, 5p, 4d and 5d) are large. Hence $\mathcal{U}$, the on-site repulsive interaction, is low, whereas $\mathcal{W}$, the band width, is high. Equivalently, since the orbitals overlap, the hopping is also fairly large. DFT is particularly accurate for weakly correlated materials, so its use for the theoretical predictions of topological properties in WTe_2 and in $MoTe_2$ is justified. In addition, topological properties of materials are usually robust and should not be sensitive to small error bars. It is noticeable, however, that the van der Waals interactions are not well described and small relative shifts of the bands cannot be excluded.

Figure 20(a) displays the band structure of WTe_2 along ΓX when SO coupling is not

taken into account (with the introduction of the intermediate point Σ such that $\Gamma\Sigma = 0.375\ \Gamma X$). Over the whole BZ, this band structure calculation indicates the presence of 16 Weyl nodes, half of them on the $k_z = 0$ plane, half of them out of this plane. The inset shows a band gap of ≈ 1 meV separating the valence and the conduction band, suggesting the presence of a gapless point nearby. Figure 20(b) shows the significant changes induced by SO coupling in WTe_2's band structure. When SO coupling is gradually increased, the Weyl points can move, annihilate or emerge in pairs of opposite chirality. In planes where $k_z \neq 0$, all the Weyl points disappear whereas 8 gapless points, formed by the crossing of the upper valence band with the lowest conduction band, remain at $k_z = 0$. A pair of Weyl points is presented in figure 20(c); they lie only slightly above the Fermi energy and they do not lie along ΓX. The other three pairs can be deduced by symmetry.

Figure 20 shows the evolution of the constant energy contours. From first principle calculations, all the Weyl points are located at $k_z = 0$. In the panel a, we see two halves of the electron pockets and two halves of the hole pockets. The rest can be deduced by symmetry along the $k_x = 0$ plane and along the $k_y = 0$ plane. The Chern number of the pockets in (a), at the energy E = 0 eV, is 0. We focus on part of the BZ represented in 20(a), everything has to be extrapolated by symmetry to evaluate the evolution of the full BZ. In figure 20(b), the constant energy cut is higher in energy, and one half of the hole pocket hole pockets disappears, and one whole hole pockets remains. Figure 20 (c), (d), (e) represent the rectangle displayed in panel (b) zoomed in, and for different energy contours. Panel c shows the lower energy Weyl point, where an electron pocket and a hole pocket touch. In panel (d), the energy is between the two Weyl points: the Chern number of the hole pocket is +1 whereas the one of the electron pocket is 0. The topology of the other hole pockets can be deduced from this Chern number: a mirror symmetry or a glide symmetry flips the sign of the Chern number. From E = 0.058 eV, the energy of the second Weyl point (panel (e)), all pockets have zero Chern number. The surface state should emerge from the pockets having non-zero Chern number.

However, it is noticeable that the distance between Weyl points of opposite chirality is only ≈ 0.7 % of the reciprocal lattice vectors. The number and arrangement of Weyl points in the BZ is very sensitive to the details of the crystal structure, leading to a different character of surface states (topological or not). In particular, weak external perturbations, may already cause changes in the band ordering, that could lead to a topological phase transition and a disappearance of the Weyl nodes. For example, temperature variations or strain may lead to a change in the lattice parameters significant enough to make the Weyl points annihilate each other.

Figure 21 shows a similar calculation for $MoTe_2$. Panel (a) displays the crossing of the electron and hole pocket required for the type II Weyl semi-metal state. Just like in WTe_2, these crossing occur slightly above the Fermi level and appear at $k_z = 0$. The difference between the two materials is that, because of the smaller size of the Mo atoms, the separation of the Weyl nodes in **k**-space should be larger. This means that the type II Weyl semimetal state should be more robust.

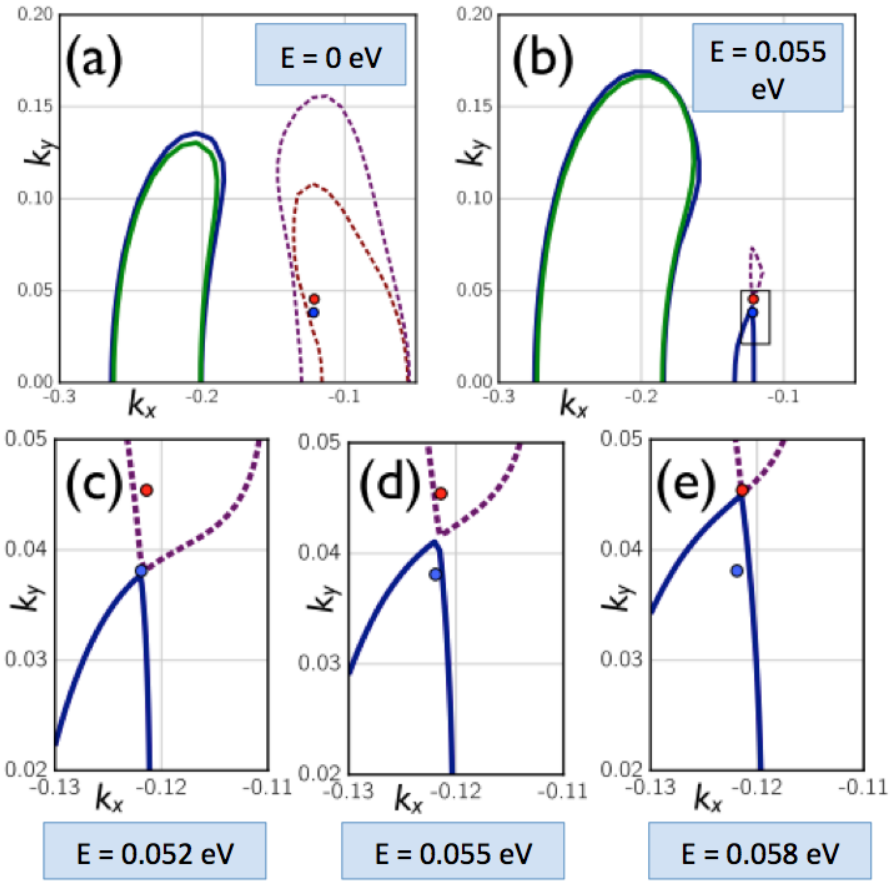

Figure 20: Theoretical prediction of Weyl nodes in WTe_2. The figure shows the Fermi surface at $k_z = 0$, as calculated by [22]. The solid lines represent the electron pockets and the dotted lines represent the hole pockets.

In figure 21(b), the elliptical contour along the [001] axis around the Weyl point W2 in the plane (k_x, k_y) marked with a black circle is the basis for a one dimensional Fermi surface. In the one dimensional dispersion plot, the band structure topology can be analyzed.

The valence band (VB) and the conduction band (CB) are gapped at all **k**-points on the cylinder. Thus, a Chern number can be calculated for the occupied states, and is found to be +1 [30]. This corresponds to the chirality of W2 and leads to the existence of a chiral edge state at the boundary between those two environments, as marked by the thin pink line denoted CTSS. The calculation predicts that this state crosses the Fermi level close to the VB.

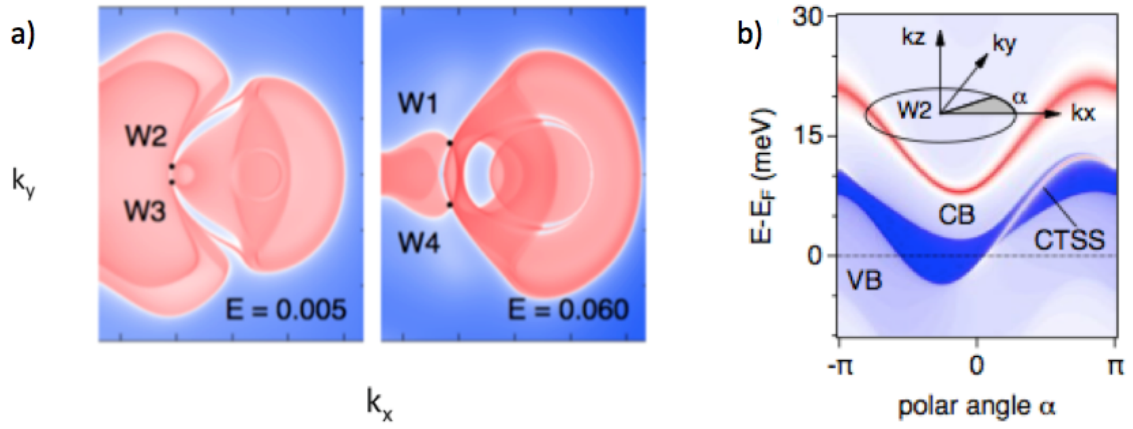

Figure 21: Theoretical prediction of Weyl nodes in $MoTe_2$. Figure (a) shows the surface density of state of constant energy contours at E = 0.005 eV and at E=0.060 eV, where the two crossings of the electron and hole pockets appear, from [30]. Those crossings have to occur at at $k_z = 0$. Figure (b) displays the Fermi arcs in $MoTe_2$. The figure shows the surface density of states along an one-dimensional elliptical contour around the Weyl point W2, from [30].

Part II
Methods

3 Materials growth and characterization

The growth of both $MoTe_2$ and $Mo_xW_{1-x}Te_2$ has been made by Céline Barreteau (from the Optics and Crystal Growth of the University of Geneva) using an optimized Chemical Vapour Transport described in [30] with $TeCl_4$ used as a transport agent, according to the following equation:

$$2(\frac{\mathrm{n}-1}{\mathrm{n}})\mathrm{Te} + (\frac{1}{\mathrm{n}})\mathrm{TeCl_4} + \mathrm{Mo} \longrightarrow \mathrm{MoTe_2} + (\frac{3}{\mathrm{n}})\mathrm{Cl_2}$$

The mixture is sealed in a quartz tube under vacuum ($5 \cdot 10^{-6}$ mbar), as shown in figure 22. This tube stayed in this two zone furnace for one week.

$MoTe_2$ spontaneously crystallizes in the 2H phase. In order to have the orthorhombic structure, the growth has to be made at high temperature. At the hot spot (980°C), the reaction compounds Mo, Te and $TeCl_4$ become volatile (left part of figure 22). The right part of the quartz tube, which is colder, acts as a cryopump: when the materials reach

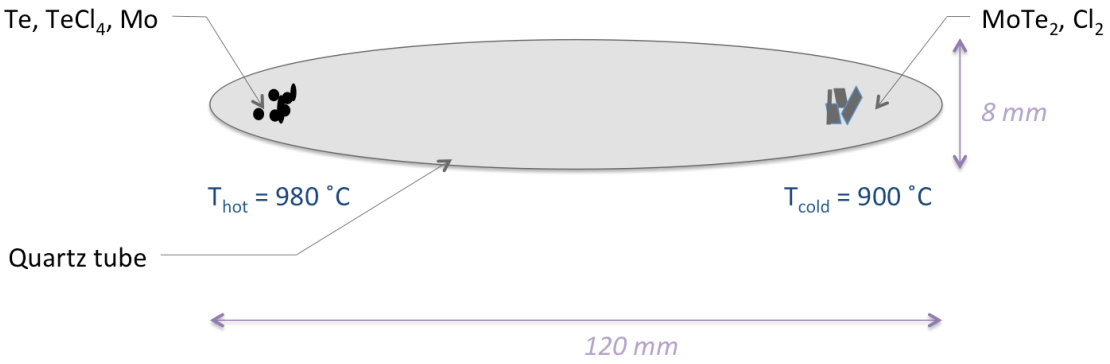

Figure 22: Illustration of the chemical vapour deposition technique used for the growth of 1T' $MoTe_2$ single crystals. The reaction compounds in stoichiometric conditions become volatile when they reach the temperature of the hot spot (980°C) and crystallize at 900°C.

the temperature of 900°C, they crystallize in their most favorable structure which is 1T'. The crystal growth should be slow enough to enable the formation of big crystals. Small crystalline areas are due to a multiplication of formation centers when the growth is too rapid. The material is prevented from changing its structure to the 2H phase by quenching it at ambiant temperature instead of making a ramp of 300°C or 400°C an hour.

WTe_2 and $Mo_xW_{1-x}Te_2$ were grown using a similar process. As Mo is smaller than W, it is easier to dope WTe_2 than the opposite. The isoelectronic substitution of the Mo atoms with the W atoms in the Td-$MoTe_2$ was not a success: the W atoms do not integrate in the structure and form clusters.

All samples were shiny dark grey and rectangularly shaped.

X-Ray Diffraction In order to determine the lattice parameters of 1T'-$MoTe_2$, X-ray diffraction experiments were performed by Céline Besnard from the School of Chemistry and Biochemistry of the University of Geneva.

When X-rays are elastically scattered by a crystal, there is constructive interference when the angle θ between the incident beam and the crystal plane and the beam wavelength λ follow Bragg's law.

$$2d\sin(\theta) = n\lambda \tag{42}$$

with d is the inter-atomic distance and $n \in \mathbb{N}$. Figure 23 illustrates schematically this law.

Each plane is reflecting 10^{-1} % to 10^{-3} % of the incident monochromatic radiation. As

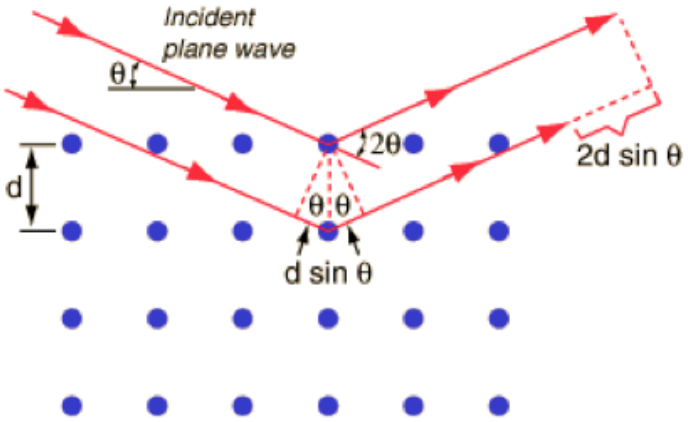

Figure 23: Geometrical explanation of Bragg law. The path difference between the two first planes is $2d\sin(\theta)$. The waves will undergo constructive interference if and only if the path difference is an integer value of the beam wavelength.

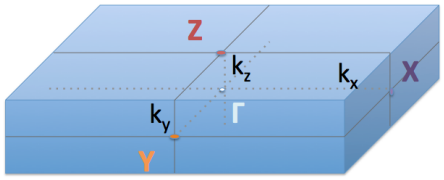

Figure 24: Brillouin Zone for WTe_2 and for $MoTe_2$. ΓX and ΓY are much longer than ΓZ.

a result, 10^3 to 10^5 planes contribute to the formation of the reflected beam. The sample is scanned by an X-ray detector through a wide range of angles 2θ and the diffraction peaks are converted to d-spacings.

The lattice parameters have been measured for several temperatures, from 230 K to 100 K. The thermal expansion coefficient of common metals and common alloys is negligible from 100 K to 10 K, so the lattice parameters used for the calculations were the one found at 100 K. The relevant parameters obtained by X-Ray diffraction for $MoTe_2$ are a= 3.468 $Å^{-1}$, b=6.310 $Å^{-1}$ and c=13.861 $Å^{-1}$. The bulk Brillouin Zone can be schematized by a parallelepiped, as shown in figure 24.

Low Energy Electron Diffraction We use this method to orient the sample before analyzing it with ARPES. A suitable cleave for ARPES experiments gives a LEED pattern

composed of a regular array of shiny dots, as shown in figure 25, whereas the pattern of samples composed of many multi-crystalline areas consists of a random sky-like ensemble of dots. In Figure 25, we confirm that the sample cleave is oriented along the (ab) plane, where the bonding with the next layer is of van der Waals type.

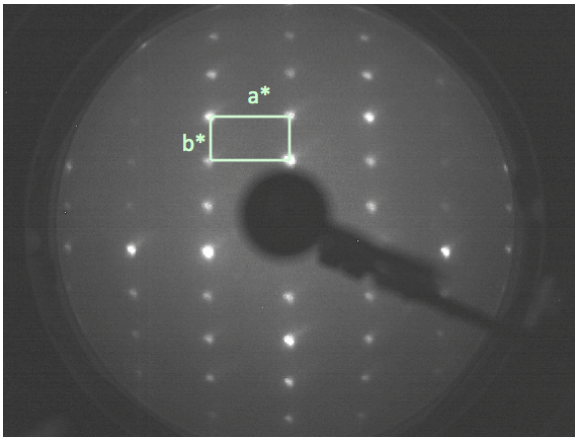

Figure 25: LEED of a Mo doped WTe_2, taken with a beam energy of 319.5 eV using a LEED from Omicron. In the LEED pattern, we recognize the reciprocal lattice vectors associated with the lattice parameters a and b, marked in light green.

4 Angle Resolved Photoelectron Spectroscopy (ARPES)

ARPES gives insights into fundamental solid state physics by directly probing the energy momentum dispersion of charge carriers, allowing to probe emergent physics of topological materials.

In all metallic compounds, determining exactly the Fermi surface is of primary importance since its shape provides valuable information on the materials electrical properties.

4.1 Introduction

Photoemission spectroscopy is based on the photoelectric effect, which is the emission of an electron from a material following the absorption of a photon. We consider here a semi-infinite crystal.

The three-step model Conceptually, it is useful to break the photoemission process into three distinct and independent steps to interpret the experiments, as described by [31]:

- **Photoionization**: In the bulk, locally, there is an optical excitation between the initial and the final Bloch state thanks to the absorption of a photon.
- **Propagation**: The electron that has been excited into the bulk final state travels and reaches the surface.
- **Escape**: The excited electron passes through the surface potential barrier and escapes into vacuum, becoming a photoelectron. In the kinematics of photoemission, this surface potential barrier the electron has to overcome to go from the surface to a point in vacuum will be called the materials work function and will be denoted ϕ.

This separation enables us to consider a Bloch state instead of a time-reversed LEED state, simplifying the interpretation of the data. Actually, photoemission is rather a one step process that consists of many-body wave functions that must obey appropriate boundary conditions (a wave matching) at the surface of the solid. Figure 26 gives a representation of the difference between the three-step model and the one-step model.

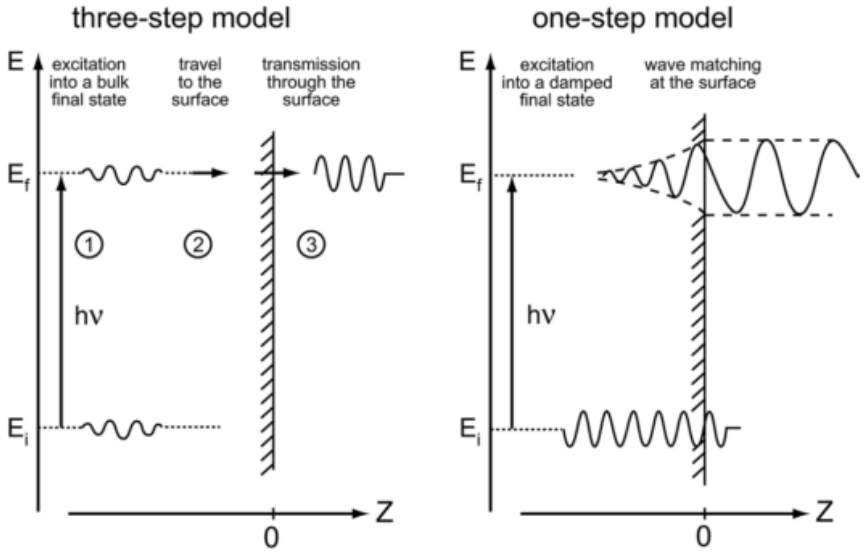

Figure 26: Sketch illustrating the differences between the 3-step model and the one-step model, from [31]. Z denotes the out-of-plane component.

The initial state is one of the possible N electron eigenstates of the semi-infinite crystal. In addition to one of the eigenstates of the ionized (N-1)-electron semi-infinite crystal, the final state has to contain the escaping electron in the form of a propagating plane wave in vacuum.

Surface states ARPES is a surface sensitive technique. As a result, it is sensible to states that exist only at the surface, to bulk states modified by the material relaxation close to the surface and finally to bulk states from a few lower layers, since the escape depth of the electrons is relatively small.

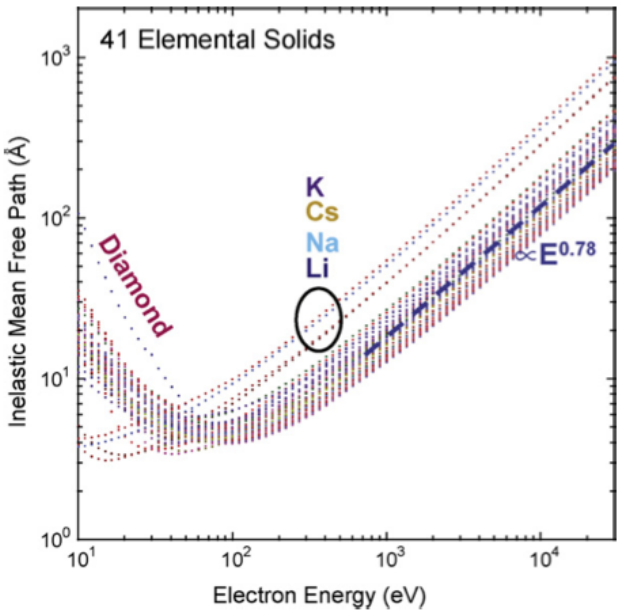

Figure 27: The photoelectron inelastic mean free path gives an idea of the depth of sensitivity in a solid sample, depending on the material investigated, from [32]

To demonstrate the existence of surface states, one has to show that the state does not disperse in k_z over the whole BZ, just like the one described figure 12(a) in the previous section.

Not all surface states are topological. Some of them can arise from changes in the electronic structure from the bulk material to the vacuum, for example. As a result, in our study, special caution should be taken to ensure that the surface states detected are topological.

4.2 Kinematics of photoemission

We use a spectrometer that simultaneously images the energy and emission angle of the emitted electron. Energy and momentum conservation enables us to deduce the momentum and the binding energy E_B the electron had in the material. When it is excited by a radiation and is ejected in vacuum, the photoelectron has a kinetic energy that depends on

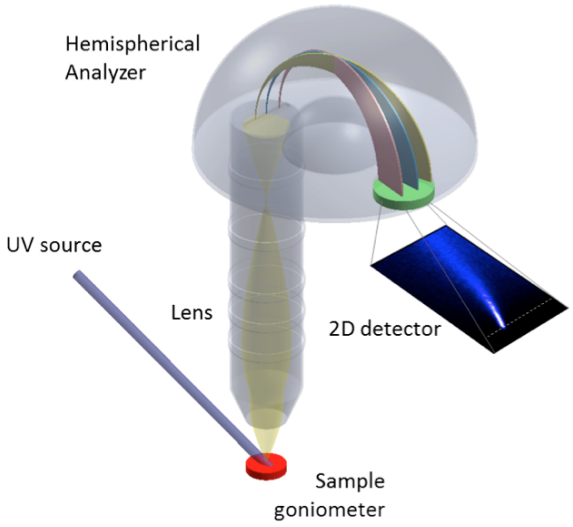

Figure 28: Sketch of a spectrophotometer detecting the angles and the energy of the electrons.

the energy of the exciting beam $h\nu$ and on the work function ϕ of the material described in the previous paragraph. Equation 43 describes the energy balance of the photoemission process.

$$E_{kin} = h\nu - \phi - E_B \tag{43}$$

The electronic dispersion in $\mathbf{k}$ space is obtained with momentum conservation. In vacuum, where the electron is free, the photoemitted electron has a momentum equal to $\frac{1}{\hbar}\sqrt{2m_e E_{kin}}$, where $\hbar$ is the reduced Planck constant and m_e is the electron mass. In the bulk, we can make a distinction between the in-plane momentum $k_{\|}$ and the out-of-plane momentum $k_{\perp}$ by writing $\mathbf{k} = \mathbf{k}_{\|} + \mathbf{k}_{\perp}$. If the photon momentum is negligible compared to the one of the photoelectron (which is usually true), $k_{\|}$ can be written as:

$$k_{\|} = \frac{1}{\hbar}\sqrt{2m_e E_{kin}} \cdot sin(\theta) \tag{44}$$

where θ is the angle at which the photoelectron is emitted measured from the surface normal. The situation is more complicated for the out-of-plane component: one has to take into account the breaking of the crystal translational symmetry in the direction perpendicular to the surface, causing the non-conservation of the out of plane component across the surface. We can approximate the bulk final state inside the crystal as free-electron like and introduce V_{in}, the inner potential, which is a barrier at the surface that prevents the

valence electrons from escaping. This potential can be determined experimentally, and is around 13 eV in metals.

Assuming the final state inside the solid to be free electron like, we have:

$$E_{kin}^{solid} = \frac{\hbar^2}{2m_e} \cdot (k_{\parallel}^2 + k_{\perp}^2) + V_{in} \tag{45}$$

Then, with the free electron final state approximation, one can write for the out of plane component:

$$k_{\perp} = \frac{1}{\hbar}\sqrt{2m_e E_{kin} \cdot cos^2(\theta) + V_{in}} \tag{46}$$

Using equations 44 and 46, the band structure of materials probed by ARPES at a given photon energy can be recovered. The photocurrent density is then proportional to the one electron spectral function weighted by the Fermi function. However, while extracting information from an experiment, one should bear in mind that the photoemission intensity also contains a one dipole matrix element equal to $\langle \Phi_f^k | \frac{e}{mc}\mathbf{A} \cdot \mathbf{p} | \Phi_i^k \rangle$, where Φ_i^k and Φ_f^k are the wave functions of the electron with momentum $\mathbf{k}$ in the initial state and final state, respectively, $\mathbf{A}$ is the electromagnetic vector potential and $\mathbf{p}$ is the electronic momentum operator. As explained in reference [31], this matrix element adds a dependence of the experimental data on the polarization direction of the vector potential $\mathbf{A}$, on the photon energy and on the geometry of the experiment. This means that, depending on their orbital character, some bands might not appear for a given vector potential. This complicates the interpretation of the data; in particular, it is difficult to estimate the size of the electron and hole pockets for a 3D material.

4.3 ARPES instruments used in this study

To avoid contamination, ARPES requires ultra high vacuum. Thermal broadening of the bands can be avoided by cooling down the sample to temperatures below 10 K. The electron spectrometer, shown schematically in figure 28, consists of an electron lens that focuses the photoelectrons at the entrance of the analyser, a hemispherical analyser that performs the energy dispersion and a phosphor screen that detects the electrons.

University of Geneva A three step process is needed to move samples from ambiant air to the analysis chamber, where the measurements are performed. The load lock can be vented with nitrogen to ambiant pressure, enabling the loading of samples. When pumped, this load lock reaches pressure of 10^{-7} mbar and can be opened to the preparation chamber, where the pressure is around 10^{-10} mbar. In the analysis chamber, where the LEED, the surface deposition and the ARPES measurements can be done after cleaving, the pressure is around 10^{-11} mbar.

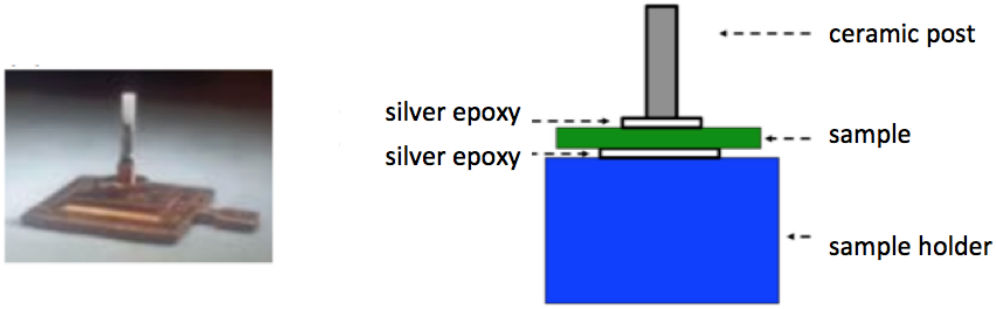

Figure 29: A sample mounted with a ceramic post, adapted from [24].

The exciting photon beam is made by a frequency converted diode laser producing a continuous wave radiation with 206 nm wavelength (6.01 eV), focused on 5 μm diameter. This implies a mean free path of $\approx$ 30 Å for the electron. Because of the relatively small photon energy, only part of the BZ can be probed for WTe_2 and $MoTe_2$. The momentum resolution is improved and reaches 0.003 $Å^{-1}$, the energy resolution being $\approx$ 2 meV. Two other radiation sources are available at the laboratory of the University of Geneva: a Helium discharge lamp providing a 40.8 eV radiation and an 11 eV laser.

The particularity of our MBS spectrometer used in our laboratory is that it permits 2 dimensional k-space scans without rotating the sample.

Synchrotron based experiments: I05 beamline at the Diamond Light source (Didcot) and HRPES beam line at the Swiss Light source (Villigen) The advantages of a synchrotron radiation is that one can vary the photon energy by changing the gap between the magnets in the undulators. As this photon energy varies from 20 to 150 eV, the mean free path for the electron is below 10 Å. The energy and momentum resolutions in the I05 beamline are 15 meV and 0.02 $Å^{-1}$, respectively. By measuring at different photon energies, one can determine the band dispersion at different k_z values and isolate the surface states from that of bulk 3D bands.

4.4 Sample Preparation and data acquisition

The quality of ARPES data acquired is sensitive to the sample quality and to the sample preparation. In particular, a contaminated sample, the presence of many small crystallites with different azimuthal orientation or chemical inhomogeneities on the sample may result in unsharp spectral features.

In order to have the sharpest signal, contaminations at the surface need to be avoided. These contaminations can come from impurities that diffuse to the surface from within the

bulk, or from the residual gas in the chamber. To minimize the latter, samples are cleaved under ultra high vacuum (of the order of 10^{-11} mbar in the laboratory of the University of Geneva), using a the ceramic post, as shown in figure 29.

As ARPES is based on the emission angle, one is interested in having possibly flat samples, just like the one in figure 30(a). If the sample is not flat, then the emission angle changes as soon as the laser spot moves on the sample, so constant adaptation of the sample orientation is needed. In addition, a flake that comes out of the sample is only weakly connected to the rest of the sample: this creates a bad thermal contact, thus a thermal broadening of the features and additionally a charge abnormality that deviates the photoelectrons and distorts the acquired data. Finally, the layered structure of the

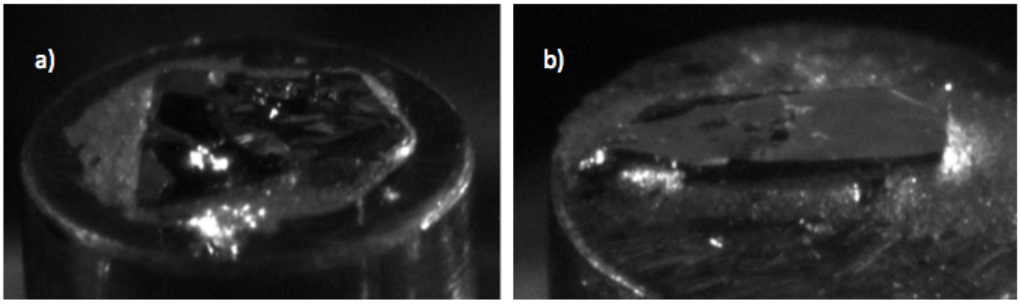

Figure 30: Two cleaved samples of Mo doped WTe_2. Due to the layered structure of the materials, most cleaves looked like the one panel a, whereas the surface needed to use ARPES should be flatter and more homogeneous, like the cleave in panel b.

materials we are investigating is also responsible for the stacking faults present in WTe_2, $MoTe_2$ and $Mo_xW_{1-x}Te_2$. Typically, there are multi-crysalline areas of ≈ 50 μm diameter whose relative orientations are slightly different. This also requires contant adaptation of the sample orientation during the measurements. Such an adaptation is especially difficult during the acquisition of a Fermi surface at the synchrotron, where the angle has to be changed and the position has to be tracked down.

5 Energy Dispersive X-Ray spectroscopy

In scanning electron microscopy (SEM), primary electrons with energies at 0.1 keV to 50 keV interact with the sample and produce backscattered electrons, Auger electrons, secondary electrons and X-Rays. For the measurements that we have done, the electrons were accelerated through a voltage difference equal to 20 keV. The emission of characteristic X-Rays can be used by the energy dispersive spectrometer to determine the chemical composition of the sample area probed by the SEM. The energy levels of the emitted X-

Rays are then associated with the elements and the shell levels that generate them. Because of the high mass of W, Mo and Te, Energy Dispersive X-Ray Spectroscopy (EDX) is an appropriate technique to evaluate the atomic composition of the materials.

In my analysis, I have chosen to focus the electron beam on a series of spots to evaluate the differences in the chemical composition on localized spots of a given cleave, the spatial resolution of this technique being of the order of $\approx 1\ \mu\text{m}^2$.

Part III
Results

6 WTe_2

6.1 Electronic structure of pure WTe_2

The bulk electronic structure of WTe_2 is not fully understood to date. Given the layered structure of WTe_2, an intuitive expectation would be a band structure that is predominantly two-dimensional. However, quantum oscillation studies can distinguish a frequency for all pockets in the three high-symmetry directions, and confirming the finite extension of the electron and hole pockets at the Fermi-level along k_z implying a highly 3D electronic structure [13]. Magnetotransport and published ARPES experiments [33] [34] [35] also display a wide dispersion in the number of pockets in the Fermi surface: as an example, the analysis of the Shubnikov-da Haas oscillations in the Seebeck response of WTe_2 made by Zhu *et al.* suggested four hole-like and four electron-like pockets of three dimensional character [13], whereas the ARPES-based experiments of Jiang *et al.* evoke five hole-like and four electron-like Fermi pockets [35] while the ARPES study of Pletikosić *et al.* reports a two-dimensional electronic structure [33].

ARPES results To get more insight into the electronic structure of WTe_2, ≈ 20 samples were cleaved below 10 K in the laboratory at the University of Geneva. We noticed two different types of Fermi surfaces and dispersion cuts, with approximately 50 % chance of observing each type (figures 31, 32 and 33). Yet a difference in the chemical composition for samples showing each type of dispersion plot can be ruled out because all samples were taken from the same batch. Instead, we associate the two distinct band structures with the two inequivalent (001) surfaces. As explained in the introduction, the top and bottom (001) surfaces of the WTe_2 lattice are different because of the non-centrosymmetric crystal structure.

In good agreement with the band structure calculations, we find four hole bands near the Fermi level and two electron bands for positive k_x, the rest of the band structure (for negative k_x) can be deduced by symmetry with respect to the Γ point. However, this agreement is only qualitative. We notice in particular a variation in the dispersion of the hole band marked in dark green in figure 31. The purple arrows indicate the energy gap between the bottom of the electron pocket in light blue and the hole bands: in the band structure calculated from first principle calculations, this energy difference is twice as large as the one evaluated in the experimental data (figures 31(e), (f) and (g)).

Also, in this calculation, the inner hole pocket displayed in the light green band does not cross the Fermi level. In all our experiments, both at the University of Geneva and at synchrotrons (Diamond Light source in Didcot (UK) and Paul Scherer Institut in Villigen

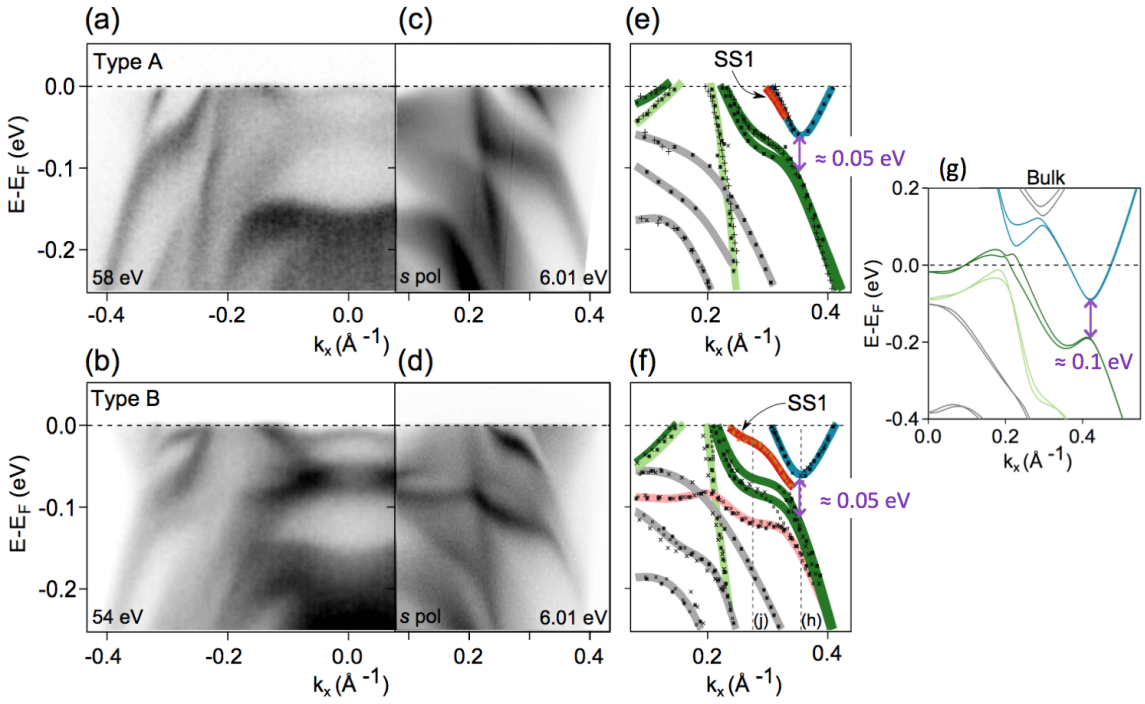

Figure 31: The two inequivalent surfaces give rise to two different dispersion plots for the (001) surface, from [6]. Panel (a), (c) and (e) display the experimental dispersion curves of a type A (001) surface. (a) and (c) show synchrotron based and laser based experiments, respectively, whereas (e) summarized extracted dispersion plots from laser based and synchrotron based experiments at several energies. Panel (b), (d) and (f) display the same experimental results, but for a type A surface. Panel (g) describes the bulk band structure of WTe_2 from first principle calculations. In panel (e), (f) and (g), the purple arrow highlights the energy difference between the bottom of the electron pocket and the position in energy of the hole pocket for the same k_x.

(Switzerland)), and for various photon energies, this hole pocket does cross the Fermi level. This discrepancy can arise from the fact that DFT is not entirely accurate in describing the van der Waals interactions between WTe_2 layer, which may result in relative shifts between different bands. The experiments also show the presence of a surface state in both types of surfaces, marked in red in figures 32, 33 and 31 and denoted SS1. This state can be clearly distinguished in the B-type surface where it connects the electron pocket to the hole pocket (see figure 31 and figure 32). In the A-type surface, we notice this state at the edge of the electron pocket, as marked in red in figure 31 and in figure 33. We confirm the surface character of the state marked in figures 31 and 32 by measuring its dispersion with

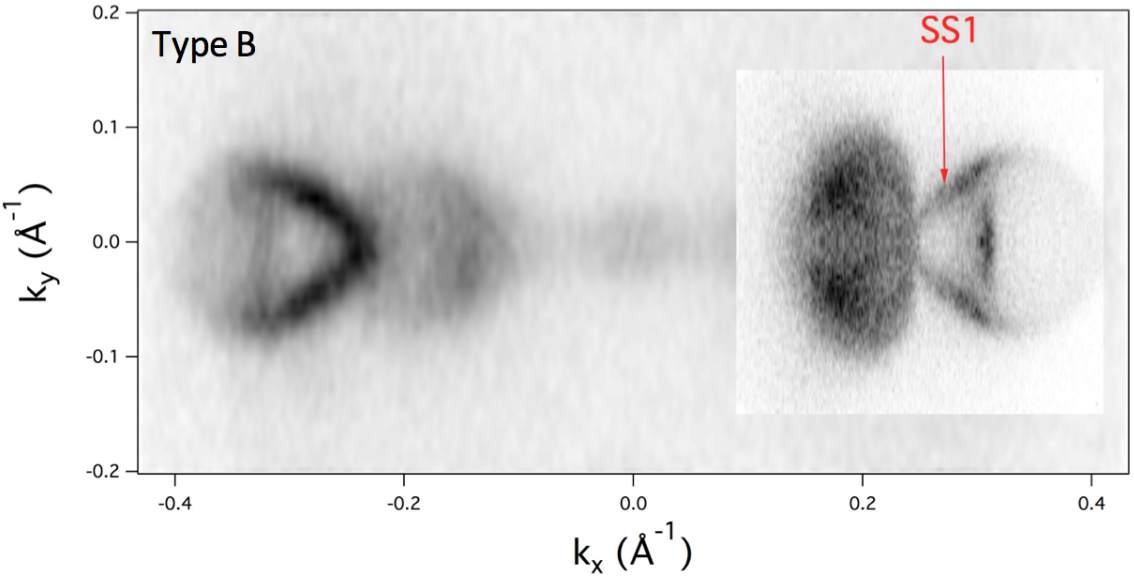

Figure 32: ARPES Fermi surface of WTe_2, taken at the Diamond Light Source with a 54 eV photon energy (left) and at the University of Geneva with a 6.01 eV photon energy (right)

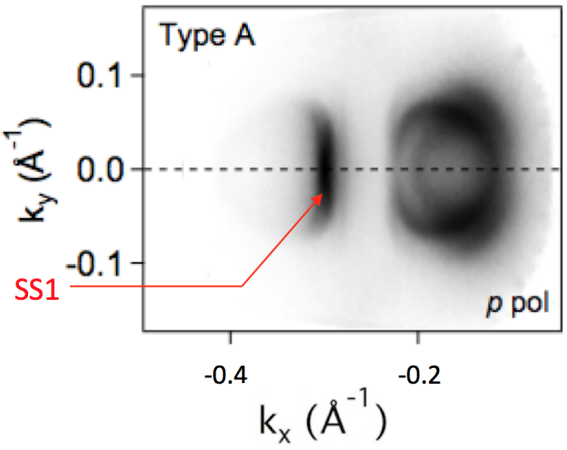

Figure 33: Laser ARPES Fermi surface of WTe_2 taken at the University of Geneva. The surface state is less visible than in the type B Fermi surface.

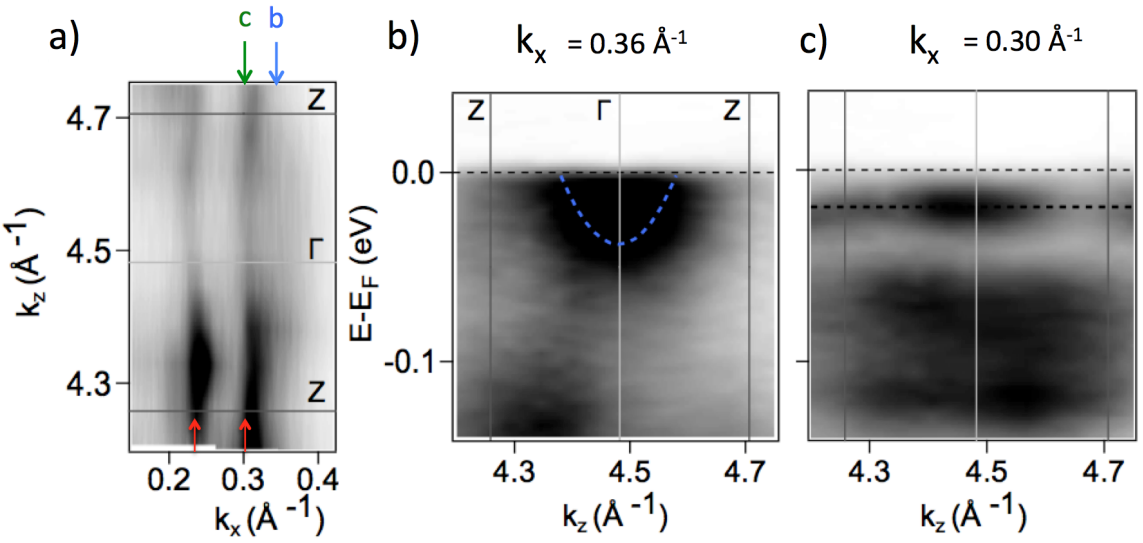

Figure 34: (a) Dispersion in the (k_x, k_z) plane measured at E=E_F, from [6]. The red arrows indicate the non-dispersive states. (b) and (c) display dispersion plots along ΓZ measured at k_x = 0.36 Å^{-1} and k_x = 0.30 Å^{-1} marked by green and blue arrows, respectively, in panel (a).

different photon energies. Figure 34(a) displays a (k_x, k_z) cut at E=E_F, where two non dispersive bands, marked by red arrows, are visible, one at k_x = 0.24 Å^{-1} and one at k_x = 0.3 Å^{-1}. The latter is marked by a green arrow in figure 34(a) and its dispersion plot along k_z is shown in figure 34(c). We identify these two surface states with the 2D states SS1 and SS2 observed in the band structure calculations shown in figure 35(a).

The determination of the dispersion along k_z enables us also to resolve the disagreement between the two-dimensional character of the band structure suggested by previous ARPES experiments [33] and the three-dimensional character established by quantum oscillations measurements [13]. In contrast to the state marked by the green arrow in figure 34(a), the state marked by a blue arrow seem to disperse along k_z. Figure 34(b) confirms the dispersive character of this state along k_z and reveals an energy dispersion of the electron pocket at k_x = 0.36 Å^{-1}, as indicated by the blue dotted line. This dispersive state along k_z demonstrates the three-dimensional nature of the electronic band structure of WTe_2.

Discussion Band structure calculations of WTe_2 predict 8 Weyl points in the k_z = 0 plane ≈ 50 meV above the Fermi level for the lattice parameters taken at 113 K [22]. The difficulty of establishing the type II Weyl semimetal state lies in the small distance between two Weyl points of opposite topological charge (the separation in **k**-space is only 0.7% of

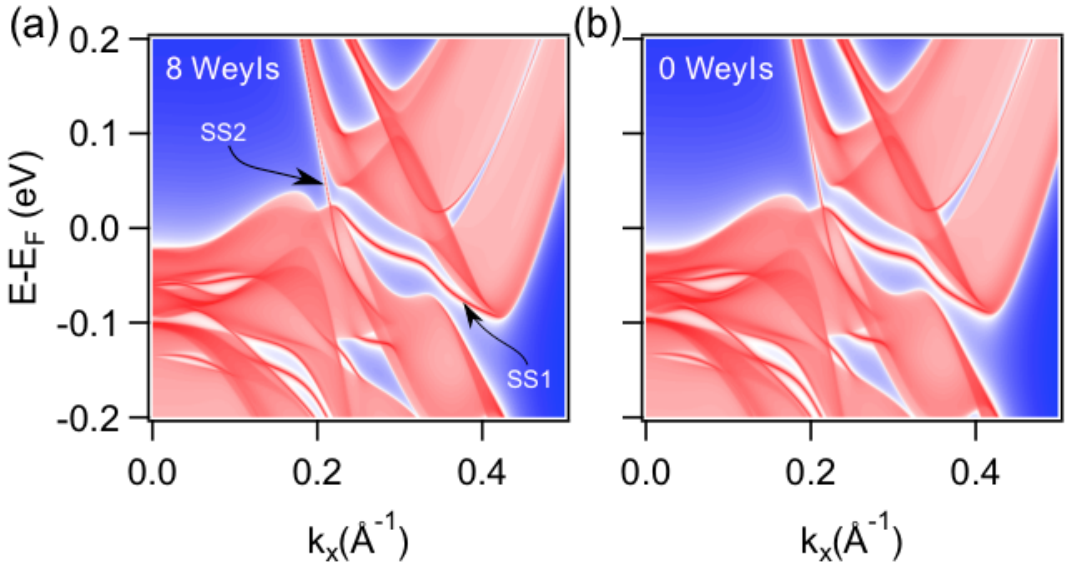

Figure 35: Surface density of states along k_x for the (001) surface. In panel (a), with the lattice parameters taken at T=113 K, there are 8 Weyl points, whereas the band structure calculated with the lattice constants at room temperature in panel (b) does not have any Weyl points, from [6]

the reciprocal lattice vector). First, a small separation between two Weyl nodes means a reduced size of the open Fermi arc connecting the two. Second, the surface state producing this arc may disappear altogether as relatively small shifts in the dispersion of neighboring bands can easily annihilate the Weyl nodes.

To evaluate the topological character of these surface states, we perform calculations of the surface density of states for two sets of lattice parameters, one at 113 K and one at room temperature (figure 35). The small change in the lattice parameters due to the temperature increase has dramatical impact on the topology of the band structure: out of the 8 Weyl nodes that existed at 113 K, none is left (figure 35(b)). In contrast, the dispersion along ΓX is nearly identical for both lattice constants. In particular, similar surface states to the one denoted SS1 and SS2 in figure 35(a) are still observable in the calculation for the structure that exhibits no Weyl nodes. Thus the existence of a surface state is not sufficient to prove the type II Weyl semimetal state. As a result, even if it is tempting to call WTe_2 a type II Weyl semimetal, the minute differences in the band structure calculations of a structure hosting 8 Weyl points and one with zero Weyl points are not noticeable with the current resolution of ARPES experiments. It is thus premature to conclude the presence of type II Weyl fermions in WTe_2 based on those results.

6.2 Surface doping of WTe_2 with Potassium

Adsorption of Potassium (K) on the surface of WTe_2 is a way to dope electrons into the system and move the chemical potential so that states that were previously above the Fermi level become accessible by ARPES. As the Weyl points are supposed to be above the Fermi level, the goal of this experiment would be to see the evolution of the band structure as we are increasing the electron doping. However, we will not be able to see the crossing of the pockets with a 6.01 eV radiation because we are not in the $k_z = 0$ plane where the Weyl nodes are. At a synchrotron as well, performing such an experiment is really difficult because the momentum resolution of the out-of-plane component does not allow a difference between the band crossing and a gap of a few meV.

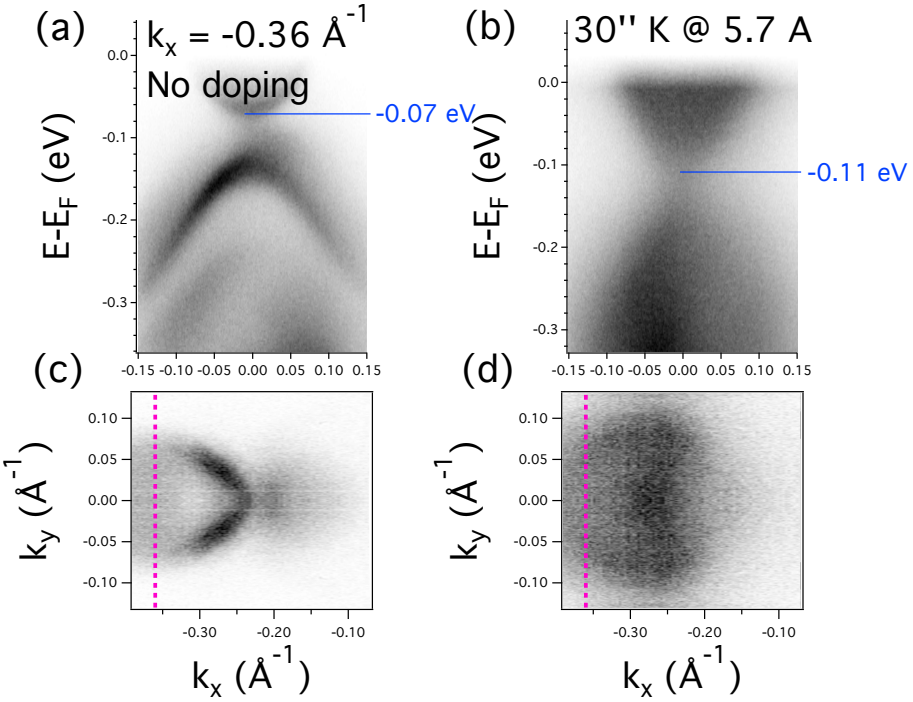

Figure 36: (a) and (b): Energy dispersion cut along IY for k_x = - 0.36 Å^{-1} of pure WTe_2 and of WTe_2 that has been doped $\approx$ 30 " with K by surface deposition. (c) and (d): Evolution of the Fermi surface with the K deposition. As expected, the hole pocket is not visible any more whereas the electron pocket became larger. The pink dotted line denotes the place in **k**-space where the energy dispersion curves have been made in (a) and (b).

We doped WTe_2 by heating a K getter five minutes at 4 A and then 5 minutes at 5.7

A. Because of the lack of a shutter on the evaporator, we reduced the K deposition on the sample during the degassing phase by making it face the side of the chamber opposite to the K getter. After this pre-heating phase, the manipulator was rotated back and we stopped the current as soon as the sample faced the K getter. Taking into account the motor velocity, we estimate the time of K deposition to ≈ 30 s. The action of K is verified in the evolution of the band structure.

We follow the positions of the dispersion bands in energy, as shown in figure 36(a) and 36(b) and notice an energy shift of ≈ 60 meV due to the surface deposition of K. As expected, the hole pocket tends to disappear whereas the electron pocket is getting bigger with electron doping: I evaluate the diameter the diameter of the latter to be ≈ 0.15 Å^{-1} along k_y for the undoped case and a diameter of ≈ 0.20 Å^{-1} along k_y for the doped case (figure 36(c) and 36(d)). While this experiment confirms that it is in principle possible to dope electrons into WTe_2 by K adsorption, further detailed experiments will be needed to understand the evolution of the band structure in the vicinity of the Weyl points.

6.3 Isoelectronic substitution of W atoms by Mo atoms in WTe_2

In the materials investigated, some W atoms are replaced by Mo atoms. We call this isoelectronic substitution and not doping because the total number of charge carriers per unit cell does not change. Since band structure calculations [36] [37] as well as ARPES experiments [30] report larger hole and electron pockets for $MoTe_2$ than for WTe_2, we expect the hole and the electron pockets to extend with increasing isoelectronic substitution of W atoms by Mo atoms.

First, this experiment is difficult because, just like WTe_2 and $MoTe_2$, the intermediate compound is a layered material and its growth by CVD results in a composition of small crystalline areas. Additionally, the intermediate compound has irregularities induced in its bulk chemical structure when W atoms are replaced by Mo atoms: the non-homogeneity of the sample composition leads to unsharp spectral features in the experimental data.

Band structure calculations of $MoTe_2$ [36] [37] predict a more robust type II Weyl semi-metal state for $MoTe_2$ compared to WTe_2 [22] since the separation between Weyl nodes of opposite chirality is larger in the former compound. As a result, if WTe_2 and $MoTe_2$ are indeed type II Weyl semi-metals, we expect the robustness of this topological state to increase with increasing isoelectronic substitution of W atoms by Mo atoms. In this case, a characteristic signature in the form of an open Fermi arc connecting the Weyl nodes should be visible. The size of this arc should increase with the Mo concentration, making the surface state easier to detect.

ARPES results In order to compare the energy dispersion, the band dispersion of the compounds with different Mo concentrations has been extracted, as displayed in figure 37. Because $Mo_xW_{1-x}Te_2$ and WTe_2 share the same structure, two inequivalent cleaving surfaces are also expected. Figure 38 shows dispersion plots along ΓX of type B surfaces

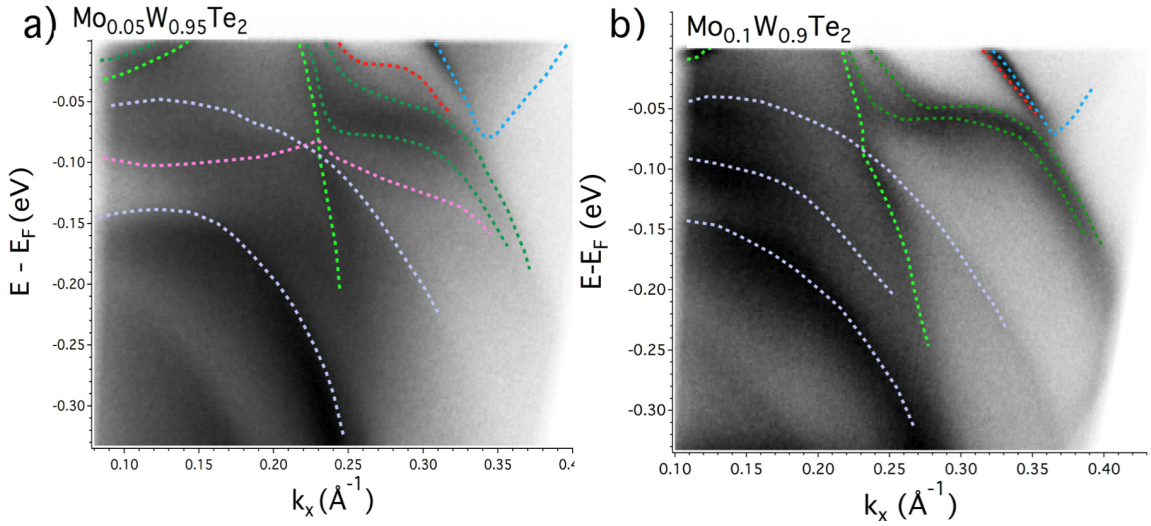

Figure 37: Extracted dispersion of the bands from measurements with the 6.01 eV excitation energy. Panel a displays a cut along ΓX for 5% nominal doping (type B) whereas panel b displays the same cut for 10% nominal doping (type A).

with different nominal dopings. In order to compare the dispersion plots, I took the crossing of a hole pocket with the Fermi level at $k_x \approx 0.215$ Å^{-1}, as circled in red in figure 38. What is noticeable is that no clear trend can be determined on this type of surface. The electron pocket on the right is closer to the Γ point with 5% doping than with no doping. But on the other hand, the same electron pocket with 10% is further away from the Γ point.

The differences we find for different Mo doping for the type A surface are similar. Within the same sample as well, comparable differences are visible. Thus from the dispersion cuts along ΓX, no clear trend can be resolved with the Mo concentration. Comparing the pocket sizes on the Fermi surfaces provides another way of comparing the electronic structures of neighboring compounds. The contours of the pockets in **k**-space have been determined and inserted in a procedure that approximates the area enclosed in each pocket. The operation in this procedure consists of adding all triangular areas formed by two neighboring points belonging to the pocket contour and the center of the pocket.

Figure 39 shows the calculated area of electron and hole pockets in the Fermi surface of samples with three different Mo concentrations, 5%, 10% and 20% using this procedure. The comparisons for all Fermi surfaces are summarized in figure 40. The tendency expected is sometimes verified, but not always. For example, the electron pockets in both type A and type B surfaces seem to increase steadily with the Mo concentration, whereas the outer hole pocket does not seem to grow as the substitution of W atoms by Mo atoms increases in the type A surface and in the type B surface, the inner hole pocket even decreases in

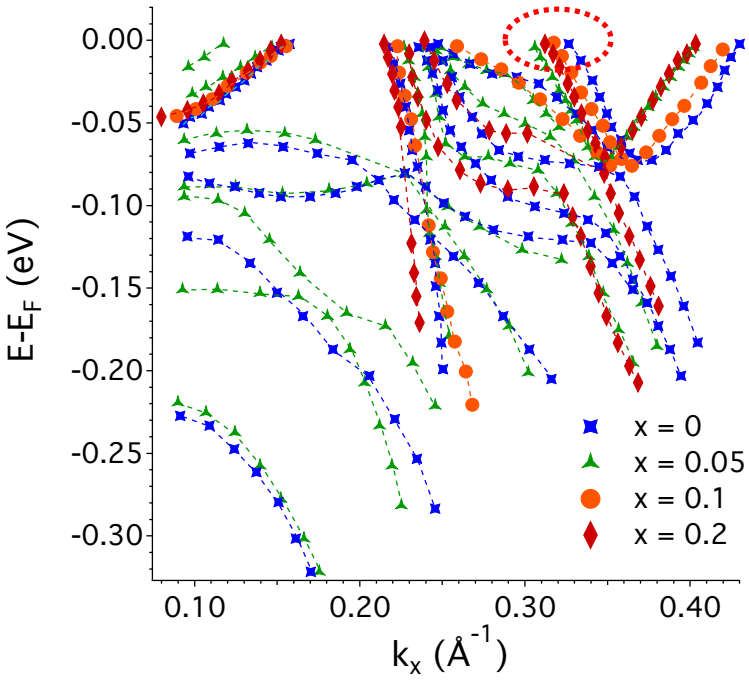

Figure 38: Dispersion relation in Mo doped WTe_2 from B-type surfaces with different Mo concentrations, denoted x. The red dotted line denotes the crossing of the electron pocket and the Fermi level referred to in the text.

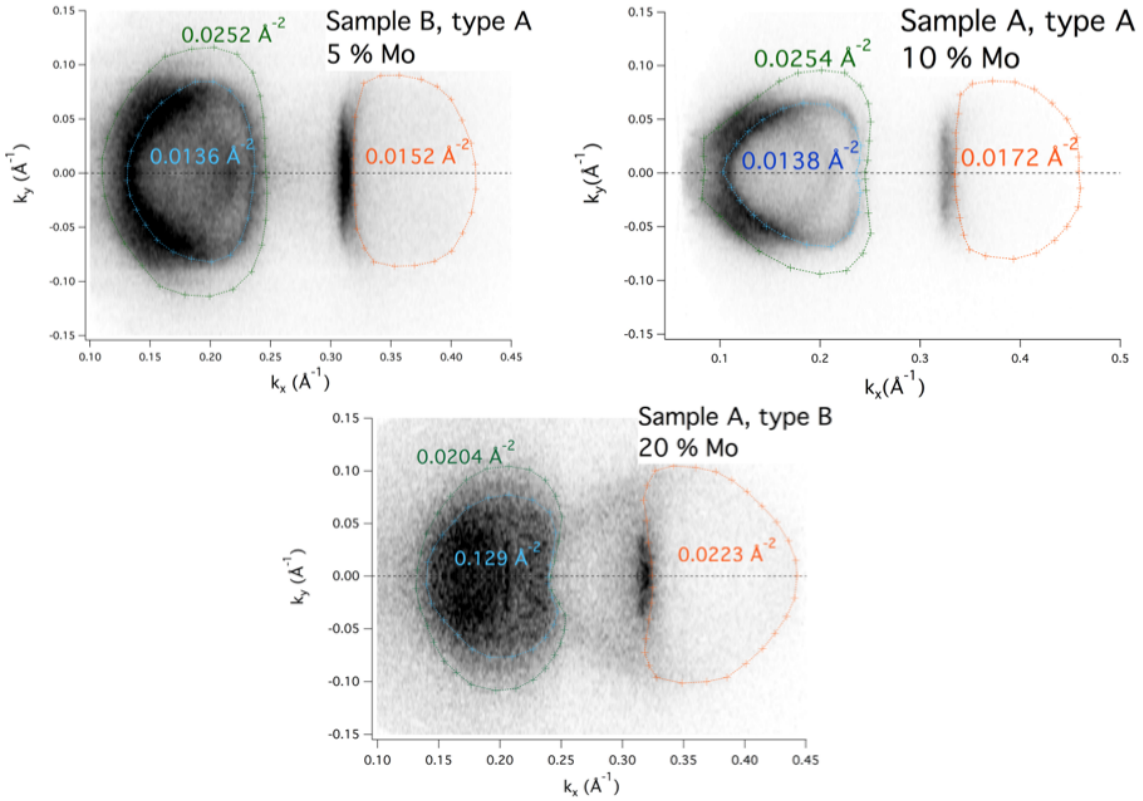

Figure 39: Different Fermi surfaces for nominally 5%, 10% and 20% isoelectronic substitution

size when the nominal doping moves from 10 % to 20 %. In addition, the difference in the electron pocket size for two type A $Mo_xW_{1-x}Te_2$ sample with 10 % nominal doping is similar to the variation found for the sample pocket with the same surface type with 5% nominal doping.

To conclude, no trend can be determined from the dispersion cuts along ΓX, but as expected, the size of the pockets seems to increase with the Mo concentration. However, discrepancies are found for the same Mo concentration, or even sometimes within the same sample. In order to understand the puzzling results at our ARPES experiments on (W/Mo)Te_2, we perform EDX measurements to map the chemical composition of our samples.

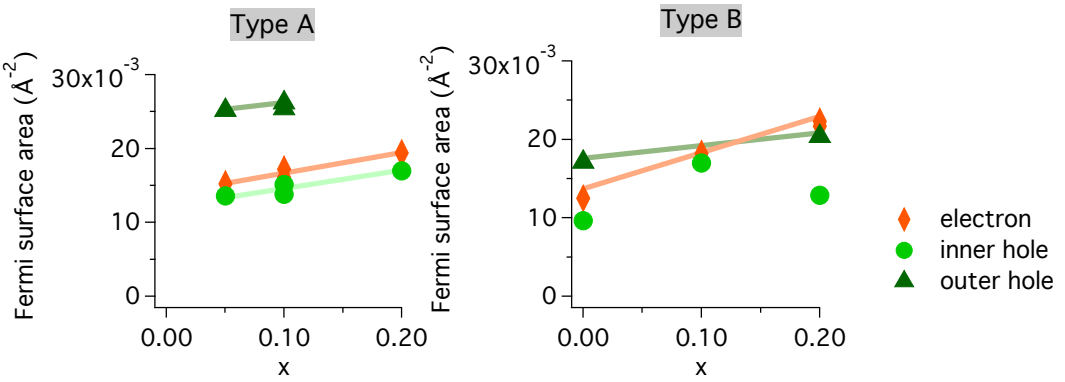

Figure 40: Evolution of the pocket sizes for nominally 0 %, 5 %, 10 % and 20 % isoelectronic substitution, denoted by x. The thick lines are guides to the eyes.

Verification of the chemical composition with Electron Dispersive X-Ray Spectroscopy (EDX) Three elements are expected in our analysis: Mo, W and Te. EDX calculates the atomic percentage of each element in the entire area of the Scanning Electron Microscope (SEM), or in a more localized area of ≈ 1 μm around a chosen spot. To determine the composition of our samples, I used $x = \frac{p_{Mo}}{p_W + p_{Mo}}$, where p_i denotes the percentage of the element i over the whole area scanned by the SEM. This is justified by the fact that Mo and W have an equivalent role in $Mo_xW_{1-x}Te_2$.

For each element, the NSS software performing the data analysis gives an error, denoted δp_W and δp_{Mo} for W and for Mo, respectively. Then the accuracy of the Mo concentration measurements is given by:

$$\delta x = \frac{|p_W \delta p_{Mo} - p_{Mo} \delta p_W|}{(p_W + p_{Mo})^2} \tag{47}$$

Typical values for this inaccuracy are of the order of $1 \cdot 10^{-2}$, and can be neglected.

Figure 41 displays one $Mo_{0.1}W_{0.9}Te_2$ sample taken with a SEM. The blue points denote the local spots at which the chemical composition has been evaluated. An additional evaluation of the Mo concentration variation has been evaluated by zooming in particular areas, as described by the colored rectangles #3, #4 and #5. For example figure 42 shows the sample area enclosed in the green rectangle # 5 in figure 41. Variations of Mo concentration arise within the same sample: in the area marked by a green rectangle, the values are approximately equal to 10 %, whereas in the area marked by an orange rectangle, the values are around 4 %. Surprisingly, the same variations are observed in the enlarged picture shown in figure 42. For example, the spot marked in orange indicates an Mo concentration of ≈ 22.4 %, whereas a neighboring point, separated by less than 25 μm, shows a concentration of $\approx 7\%$. The presence of other points with similar values for both concentrations suggest that the inhomogeneities are frequent. Indeed, those discrepancies are observed in all samples.

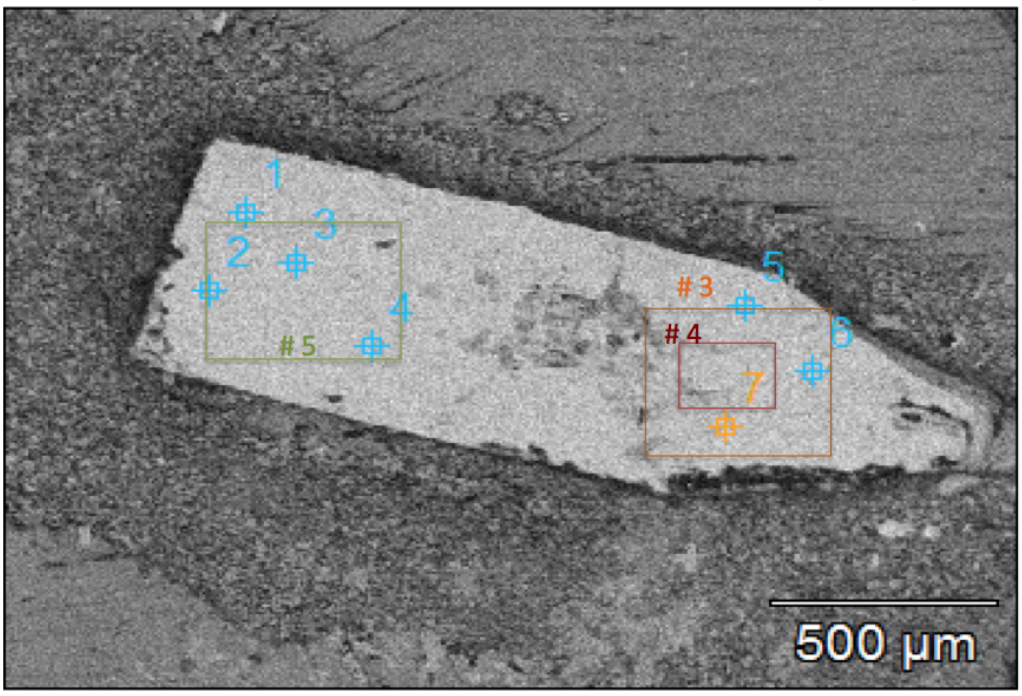

Figure 41: Variation of Mo doping depending on the location on the sample obtained using EDX, using L-lines for the mapping and the quantification, an accelerating voltage of 20 kV and the QBSD detector. The nominal doping should have been 10%. The Mo concentration in the box 5 went up to $\approx$ 22 %, whereas the Mo doping in the box 3 (displayed figure 42 is typically of the order of $\approx$ 5%).

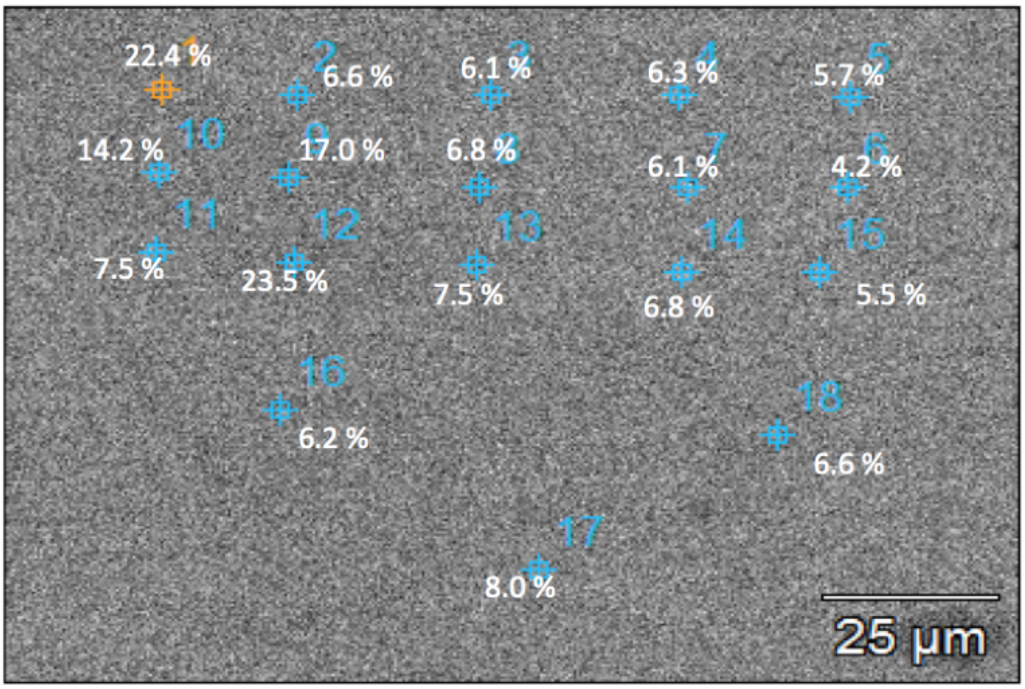

Figure 42: Spatial variation of Mo doping obtained using EDX. The area analyzed in this figure is a zoom of the area analyzed in figure 41 denoted by the green rectangle. In some spots, like the one marked with an orange cross, the Mo concentration is as high as 22 %, whereas in another spot less than 30 μm away, the Mo concentration can be as low as 7%.

In EDX, the elements are probed down to 1 μm depth, which is not the case for ARPES (of the order of 10 Å). As a result, the inhomogeneities probed with EDX are likely a lower limit of the inhomogeneities probed by ARPES. Despite this difference, changes in the chemical composition in neighboring areas within the sample are significant with EDX.

To conclude, it would be too difficult to draw any conclusion from ARPES data regarding the evolution of the band structure with Mo doping of WTe_2 because of the non reliability of the Mo concentration in the solid solutions (M/W)Te_2.

7 $MoTe_2$

$MoTe_2$ is the sister compound of WTe_2 and exists in the same Td phase at low temperature. Thus, its structure makes it a candidate for the existence of the type II Weyl semi-metal state. In the theoretical calculations done by Sun *et al.* [36] and by Wang *et al.* [37], the type II Weyl semi-metal state is predicted to be more robust because the smaller size of the Mo atoms cause the Weyl points to lie further away from each other in **k**-space. However, because of the differences in the lattice parameters used to perform the calculations, the number of predicted Weyl nodes varies: the work of reference [36] expects 8 Weyl points whereas according to the calculations of reference [37], Td-$MoTe_2$ should host 4 Weyl points. To establish the type II Weyl semi-metal state of $MoTe_2$ and to determine the correct number of Weyl nodes, we perform both synchrotron and laser based experiments and systematically compare the experimental results with the surface density of states calculated with DFT.

Since the study of WTe_2 indicated that the topology of the band structure was intimately related to the exact value of the lattice parameters, X-Ray diffraction was used to characterize the crystal structure of $MoTe_2$.

7.1 X-Ray Diffraction of 1T'-$MoTe_2$

At room temperature, the lattice parameters of the monoclinic 1T'-$MoTe_2$ are a=3.479 Å, b=6.332 Å and c=13.832 Å. Then $MoTe_2$ undergoes a structural phase transition that changes its structure at $\approx$ 240 K to the orthorhombic Td phase [5]. With decreasing temperature, the c axis expands whereas the a and b axis shrink, as described in figure 43. A linear extrapolation from the experimental values obtained from 230 K to 120 K enables the determination of the lattice parameters at 100 K used for the band structure calculations. Those values are marked by the crossing of the black line with the green, blue and red line in figure 43. The use of the lattice parameters of $MoTe_2$ at 100 K to perform band structure calculations compared with ARPES data taken below 10 K is justified by the fact that no thermal expansion is expected between 100 K and 10 K. The discrepancies between the parameters found in this work and in previous works [4] [37] also represented in figure 43 might be explained by the different conditions at which the $MoTe_2$ samples were grown.

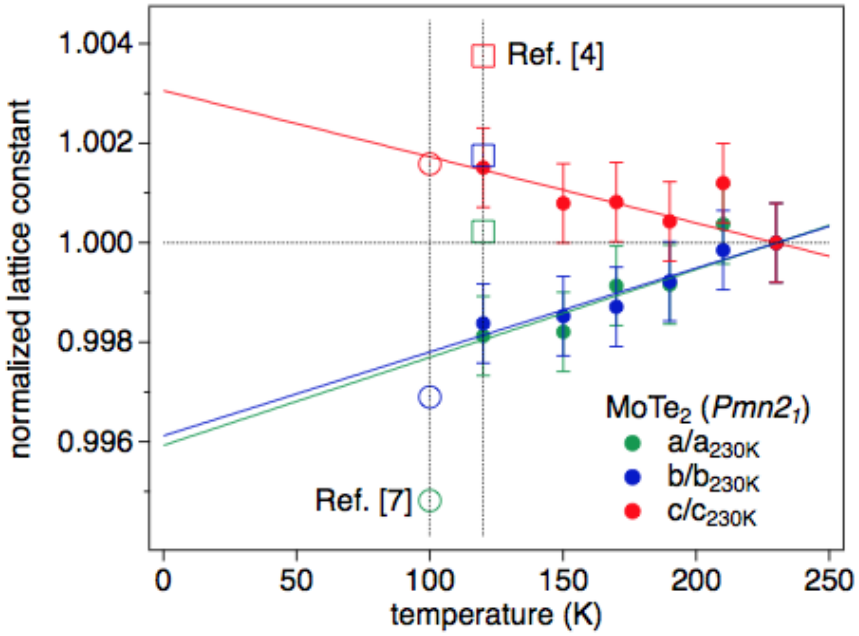

Figure 43: Temperature dependence of the lattice parameters of Td-$MoTe_2$ normalized by the values obtained at 230 K obtained with the Rigaku Supernova diffractometer. For comparison, the values of reference [4] and of reference [37] are represented by empty circles and squares, respectively.

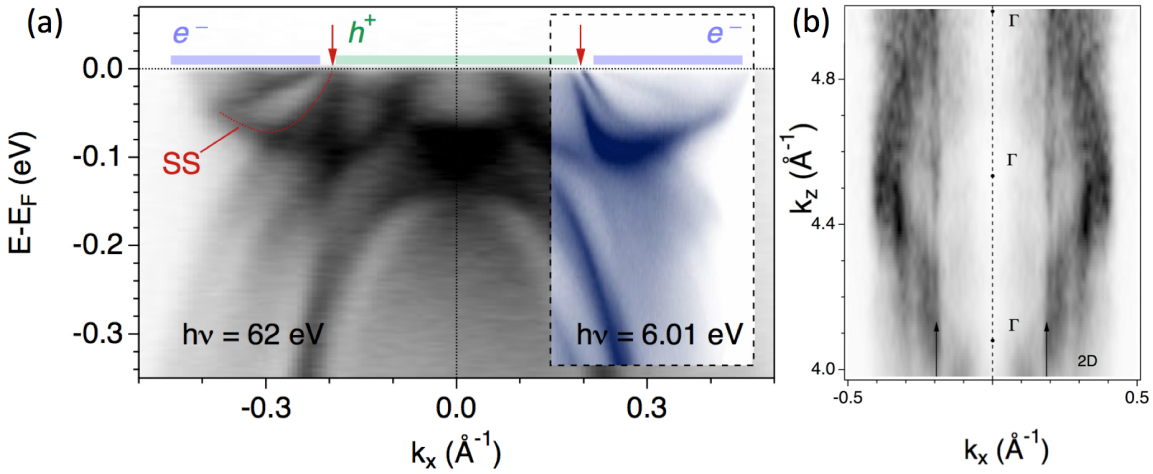

Figure 44: (a) Dispersion parallel to ΓX measured with synchrotron radiation (62 eV at the Diamond Light Source) and a laser source on $MoTe_2$ (from [30]). The red arrows indicate the surface states on both laser ARPES and synchrotron-based experiments. The green and the purple thick lines indicate the hole-like and electron-like character of the bands crossing the Fermi level, respectively. (b) (k_x, k_z) Fermi surface map taken at the Diamond Light Source. The non-dispersive states are marked by the two black arrows.

7.2 Electronic structure of pure $MoTe_2$

ARPES results Figure 44 presents the band structure of $MoTe_2$ along the high symmetry direction $k_y = 0$. A large hole like Fermi surface centered at the Γ point (marked with a thick green line) nearly touches the two electron-like pockets, symmetric with respect to the Γ point, both marked with a thick blue line. The state marked with a red line is visible in synchrotron-based experiments, but not in bulk band structure calculations, suggesting its surface character. The picture changes when laser-based experiments are performed along the same direction (in blue): we resolve two sharp dispersing states going from the bottom of the electron bands up to the top hole bands. The two states have the same Fermi velocities, but one state crosses the Fermi level, the other loses most of its spectral weight while approaching the Fermi level. To verify the 2D character of these states, a (k_x, k_z) map has been done at the Fermi level by varying the photon energy displayed in figure 44(b). The non-dispersive states, marked by black arrows, confirm the surface character of the state marked in red.

Discussion Laser-based constant energy surfaces reveal two types of Fermi surfaces, denoted surface A in figure 45(b) and surface B in figure 45(d). The difference between the A-type surface and the B-type surface is especially visible at the boundary between the

hole like and the electron like pocket. In the A-type surface, there is one surface state close to the contour of the electron pocket and two Fermi arcs with a smaller curvature on either side of the $k_x = 0$ line. On the B-type surface, one distinguishes two nearly parabolic Fermi arcs with slightly different curvatures. The calculation done with the lattice parameters

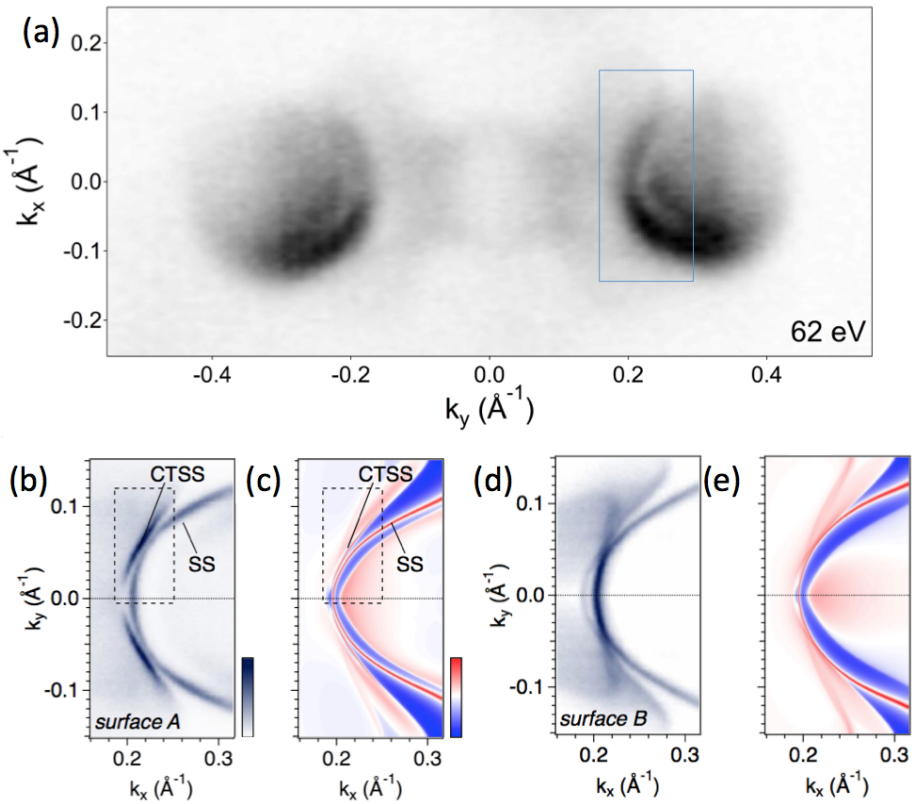

Figure 45: (a) Fermi surface measured with 62 eV photon energy and p polarization. The blue rectangle indicates the area zoomed in in panel (b), (c), (d) and (e). Panels (b) and (c) compare laser based measurements and the calculated surface density of states for the type A surface. Panels (d) and (e) display the same comparison for the type B surface, from [30].

determined at 100 K predicts 8 Weyl points in the $k_z = 0$ plane, slightly above the Fermi energy: at 0.006 eV for half of them and at 0.062 eV for the other half (the energies are taken with respect to the Fermi level). To verify the accuracy of those predictions, systematic comparisons of the experimental and calculated band dispersions have been performed. According to the calculation, the large Fermi arc close to the electron pocket is topologically trivial and even persists in calculations for structures that exhibit no Weyl

nodes. We focus then on the type A surface in figure 45(b) and (c). The shorter arc denoted CTSS in figure 45(c) represents the connection between the valence band and the conduction band crossing the Fermi level in the one-dimensional elliptical contour around the Weyl node W2 shown in figure 21(b), strongly suggesting the existence of a topologically protected state. This statement is supported by comparing the laser-based ARPES Fermi surface of type A with the calculated surface density of states in the plane (k_x, k_y) at the Fermi level in figure 45(b) and (c), respectively, where the candidate topological surface state is designated by CTSS.

Figure 46(a) and (b) zoom in the areas enclosed by a black dotted rectangle in figures 45(b) and (c), respectively. This enlarged Fermi surface enables a clearer distinction of the CTSS and strengthens the accordance between the calculations and the measurements. The cuts parallel to ΓY for different k_x values in figure 46(c) present systematic comparisons between the laser-based ARPES experiments and the calculated surface density of states and confirm the good agreement between ARPES data and numerical calculations. It is noticeable that, in contrast to WTe_2, no topologically trivial state having a similar shape as the CTSS has been found in any of our systematic band structure calculations.

The comparisons displayed in figure 46(c) indicate that the CTSS can be resolved only if it emerges out of the projected bulk hole pocket. In particular, we notice that it does not cross the Fermi level at $k_x = 0.27$ Å^{-1} in the experimental data. This renders the identification of the projected Weyl points on the Fermi surface from the ends of the topological arcs impossible.

Moreover, the calculations also indicate that the Fermi pockets have zero Chern number [30]. Thus, the emergence of the topological surface state out of the bulk hole pocket is a consequence of the shape of this state, so is actually not dictated by topology.

Additionally, when a large number of Weyl nodes exist in the band structure, hybridization can occur between the topological surface states, rendering the hybridized states topologically trivial in reality.

To conclude, the remarkable agreement between the experimental observations and the numerical calculations finding 8 type-II Weyl nodes in the band structure enables us to call $MoTe_2$ a strong candidate for the realization of a type-II Weyl semi-metal phase. This statement is confirmed by the fact that no topologically trivial scenario that could explain the experimental data has been found.

7.3 Temperature dependence of $MoTe_2$

Because of the phase transition occurring at ≈ 240 K [5], we expect to see a change in the band structure at this temperature. Since the 1T' structure does not have the symmetry required for the existence of Weyl fermions, the structural phase transition would inevitably lead to a disappearance of the CTSS. The difficulty of the experiments lies on the broad spectral features due to the high temperature that complicates the interpretation of the results.

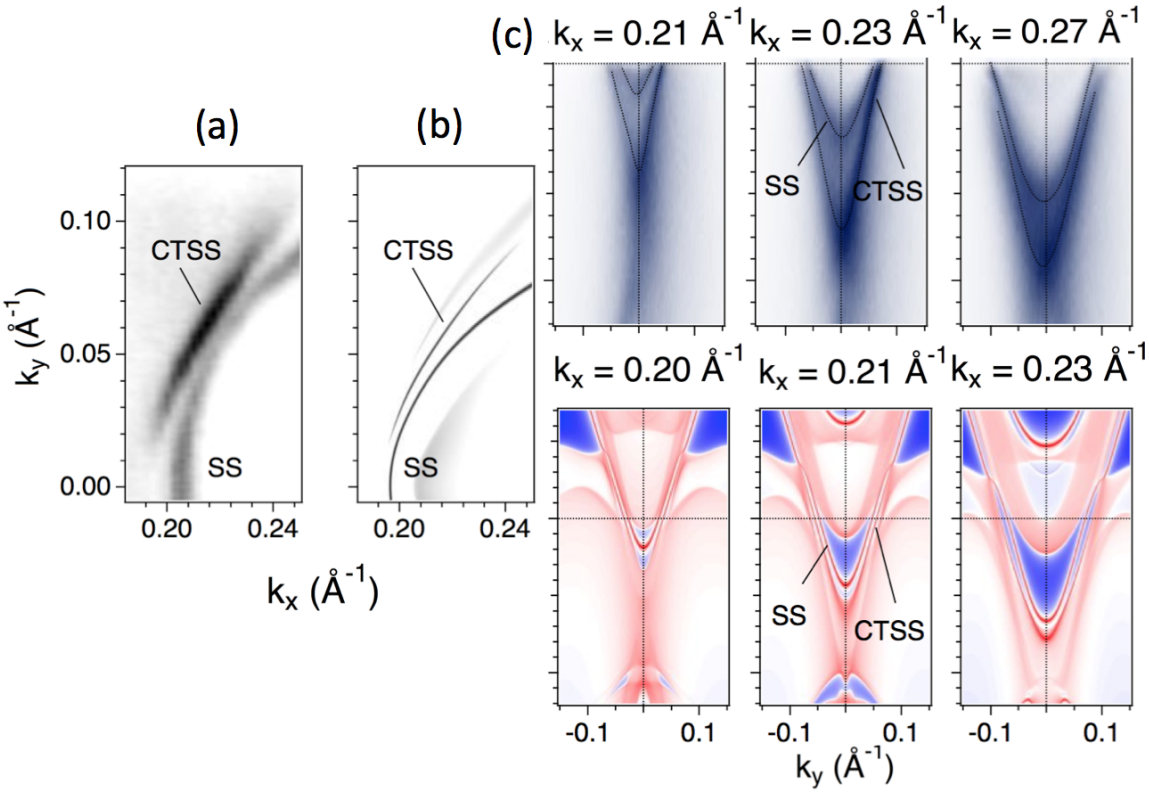

Figure 46: Comparison of experimental measurements and calculated surface band structures, from [30]. (a) and (b) are a detailed view of the Fermi surface around the CTSS marked by a black dotted rectangle in figure 45 and (c) present dispersion plots taken on surface A parallel ΓY for different values of k_x.

Dispersions plots parallel to ΓX were measured at 50 K and at 227 K, where the band structure topology should require the CTSS to stay, in contrast to the measurements done at 267 K and 284 K (figure 47). The pink line displayed in the energy dispersion at 50 K and at 284 K indicates the bulk state and the red curve named CTSS recalls the location of the candidate topological surface state identified in the previous subsection. The band structure changes a bit with the temperature: in particular, the candidate topological surface state is visible at 50 K whereas it is not anymore at 264 K. This suggests that the CTSS is indeed a topological surface state of a type II Weyl semi-metal phase that can only exist in the non-centrosymmetric Td structure.

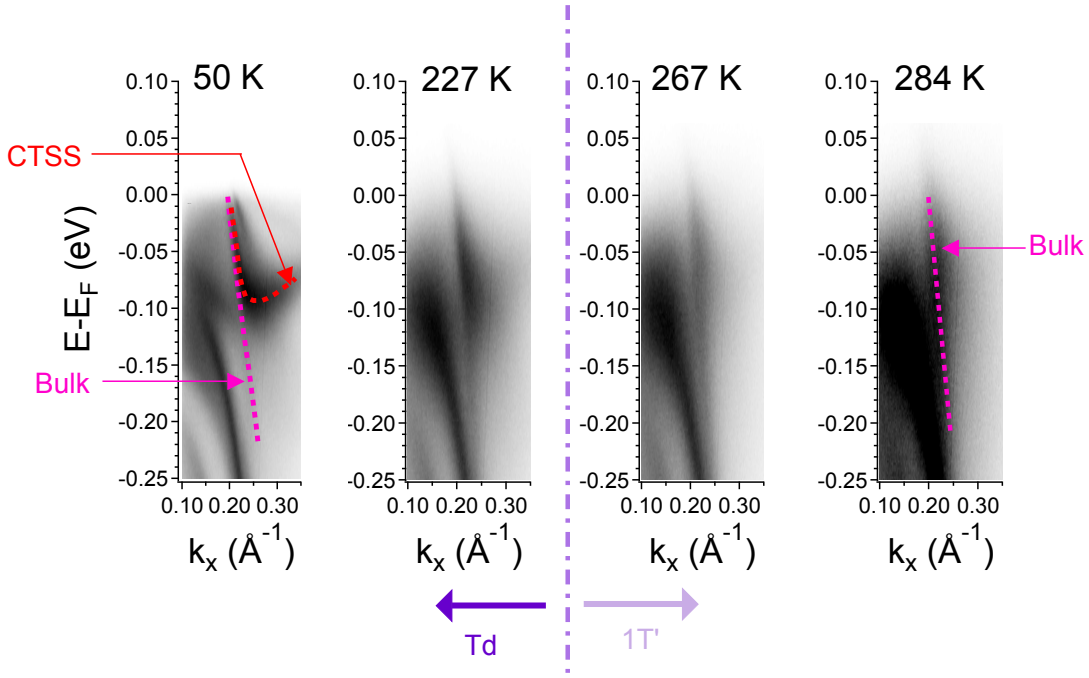

Figure 47: Temperature dependence of $MoTe_2$. At 227 K, $MoTe_2$ should still be a Weyl semimetal, and at 267 K, not anymore. The pink dotted line highlights the presence of the bulk band, present both at 50 K and 284 K. In contrast, the red state denoted CTSS at 50 K is not visible at 284 K anymore.

However, this change did not happen at a defined temperature. On the other hand, the resistivity measurements show an hysteresis over more than 100 K for the structural phase transition, giving no exact value of the temperature at which the transition should occur (see figure 3) [5].

To describe how robust this type II Weyl semi-metal state is, further measurements

need to be conducted in different **k**-space cuts where the difference between the candidate topological surface state and the trivial surface state is more visible. Smaller steps in the increase or decrease of temperature can support the link between the structural phase transition and the disappearance of the CTSS.

References

1. Chhowalla, M. *et al.* The chemistry of two-dimensional layered transition metal dichalcogenide nanosheets. *Nature Chemistry* **5,** 263–275 (2013).
2. Breuer, H., Meslé-Gribenski, M., Morin, P., Sénéchal-Couvercelle, M. & Morin, C. *Atlas de la chimie* (Librairie générale française, 2000).
3. Ali, M. N. *et al.* Large, non-saturating magnetoresistance in WTe2. *Nature* **514** (2014).
4. Qi, Y. *et al.* ARTICLE Superconductivity in Weyl semimetal candidate MoTe 2. *Nature Communications* **7** (2016).
5. Zhou, Q. *et al.* Hall-effect within the colossal magnetoresistive semi-metallic state of MoTe 2 (2016).
6. Bruno, F. Y. *et al.* Surface states and bulk electronic structure in the candidate type-II Weyl semimetal WTe 2. *Arxiv:1604.02411* (2016).
7. Neto, A. H. C., Guinea, F., Peres, N. M. R., Novoselov, K. S. & Geim, A. K. The electronic properties of graphene. *Reviews of Modern Physics* **81** (2009).
8. Hua Wang, Q., Kalantar-Zadeh, K., Kis, A., Coleman, J. N. & Strano, M. S. Electronics and optoelectronics of two-dimensional transition metal dichalcogenides. *Nature Nanotechnology* **7,** 699–712 (2012).
9. Kang, D. *et al.* Superconductivity emerging from a suppressed large magnetoresistant state in tungsten ditelluride. *Nature Communications* **6** (2015).
10. Ashcroft, N. W. & Mermin, N. D. *Solid state physics* (Brooks/Cole Cengage Learning, 1976).
11. Sondheimer, E. H. & Wilson, A. H. The Theory of the Magneto-Resistance Effects in Metals. *The Royal Society* **190,** 435–455 (1947).
12. Wang, L., Gutiérrez-lezama, I., Barreteau, C. & Ubrig, N. Tuning Magnetotransport in a Compensated Semimetal at the Atomic Scale. *Nature communications* **6** (2015).
13. Zhu, Z. *et al.* Quantum Oscillations, Thermoelectric Coefficients, and the Fermi Surface of Semimetallic WTe2. *Physical Review Letters* **114** (2015).
14. Bernevig, B. A. & Hughes, T. L. *Topological insulators and topological superconductors* (Princeton University Press, 2013).
15. Weng, H., Fang, C., Fang, Z., Bernevig, B. A. & Dai, X. Weyl Semimetal Phase in Noncentrosymmetric Transition-Metal Monophosphides. *Physical Review X* **5** (2015).
16. Hasan, M. Z. & Kane, C. L. Colloquium: Topological insulators. *Reviews of Modern Physics* **82** (2010).

17. Hsieh, D. *et al.* A topological Dirac insulator in a quantum spin Hall phase. *Nature* **452,** 970–974 (Apr. 2008).

18. Peskin, M. E. & Schroeder, D. V. *An introduction to quantum field theory* (Addison-Wesley, 1995).

19. Pal, P. B. Dirac, Majorana and Weyl fermions. *American Journal of Physics* **79,** 32 (2010).

20. Chen, Y. L. *et al.* Massive Dirac Fermion on the Surface of a Magnetically Doped Topological Insulator. *Science* **329,** 659–662 (2010).

21. Nielsen, H. B. & Ninomiya, M. The Adler-Bell-Jackiw anomaly and Weyl fermions in a crystal. *Physics Letters B* **130,** 389–396 (1983).

22. Soluyanov, A. A. *et al.* Type-II Weyl semimetals. *Nature* **527,** 495–498 (2015).

23. Wan, X., Turner, A. M., Vishwanath, A. & Savrasov, S. Y. Topological semimetal and Fermi-arc surface states in the electronic structure of pyrochlore iridates. *Physical Review B - Condensed Matter and Materials Physics* **83** (2011).

24. Xu, S.-Y. *Discoveries of New Topological States of Matter Beyond Topological Insulators* PhD thesis (Princeton Graduate Program, 2015).

25. Huang, X. *et al.* Observation of the chiral-anomaly-induced negative magnetoresistance: In 3D Weyl semimetal TaAs. *Physical Review X* **5** (2015).

26. Son, D. T. & Spivak, B. Z. Chiral anomaly and classical negative magnetoresistance of Weyl metals. *Physical Review B - Condensed Matter and Materials Physics* **88** (2013).

27. Xu, S.-Y. *et al.* Discovery of a Weyl fermion semimetal and topological Fermi arcs. *Science* **349,** 613–7 (2015).

28. Xu, S.-Y. *et al.* Discovery of a Weyl fermion state with Fermi arcs in niobium arsenide. *Nature Physics* **11,** 748–754 (2015).

29. Xu, S.-Y. *et al.* Discovery of Lorentz-violating Weyl fermion semimetal state in LaAlGe materials. *Arxiv:1603.07318* (2016).

30. Tamai, A. *et al.* Fermi arcs and their topological character in the candidate type-II Weyl semimetal MoTe2. *arXiv:1604.08228* (2016).

31. Damascelli, A. Probing the Electronic Structure of Complex Systems by ARPES. *Physica Scripta* **T109,** 61–74 (2004).

32. Fadley, C. X-ray photoelectron spectroscopy: Progress and perspectives. *Journal of Electron Spectroscopy and Related Phenomena* **178,** 2–32 (2010).

33. Pletikosić, I., Ali, M. N., Fedorov, A. V., Cava, R. J. & Valla, T. Electronic Structure Basis for the Extraordinary Magnetoresistance in WTe2. *Physical Review Letters* **113,** 216601 (2014).

34. Wu, Y. *et al.* Temperature-Induced Lifshitz Transition in WTe2. *Physical Review Letters* **115** (2015).

35. Jiang, J. *et al.* Signature of Strong Spin-Orbital Coupling in the Large Nonsaturating Magnetoresistance Material WTe 2. *Physical Review Letters* **115** (2015).

36. Sun, Y., Wu, S.-C., Ali, M. N., Felser, C. & Yan, B. Prediction of Weyl semimetal in orthorhombic MoTe 2. *Physical Review B* **92** (2015).

37. Wang, Z. *et al.* MoTe2: Weyl and Line Node Topological Metal. *arXiv:1511.07440* (2015).